

OFDM-Based Massive Connectivity for LEO Satellite Internet of Things

Yong Zuo, Mingyang Yue, Mingchen Zhang, Sixian Li,
Shaojie Ni, and Xiaojun Yuan

Abstract

Low earth orbit (LEO) satellite has been considered as a potential supplement for the terrestrial Internet of Things (IoT). In this paper, we consider grant-free non-orthogonal random access (GF-NORA) in orthogonal frequency division multiplexing (OFDM) system to increase access capacity and reduce access latency for LEO satellite-IoT. We focus on the joint device activity detection (DAD) and channel estimation (CE) problem at the satellite access point. The delay and the Doppler effect of the LEO satellite channel are assumed to be partially compensated. We propose an OFDM-symbol repetition technique to better distinguish the residual Doppler frequency shifts, and present a grid-based parametric probability model to characterize channel sparsity in the delay-Doppler-user domain, as well as to characterize the relationship between the channel states and the device activity. Based on that, we develop a robust Bayesian message passing algorithm named modified variance state propagation (MVSP) for joint DAD and CE. Moreover, to tackle the mismatch between the real channel and its on-grid representation, an expectation-maximization (EM) framework is proposed to learn the grid parameters. Simulation results demonstrate that our proposed algorithms significantly outperform the existing approaches in both activity detection probability and channel estimation accuracy.

Index Terms

GF-NORA, LEO satellite-IoT, joint DAD and CE, Bayesian message passing, expectation-maximization.

Yong Zuo and Shaojie Ni are with the College of Electronic Science and Technology, National University of Defense Technology, Changsha, China (e-mail: zuoyong@nudt.edu.cn; nishaojie123@126.com).

Mingyang Yue, Mingchen Zhang, Sixian Li and Xiaojun Yuan are with the National Laboratory of Science and Technology on Communications, University of Electronic Science and Technology of China, Chengdu 611731, China (e-mail: {myyue, zhangmingchen, sxli}@std.uestc.edu.cn; xjyuan@uestc.edu.cn).

This work has been submitted to the IEEE for possible publication. Copyright may be transferred without notice, after which this version may no longer be accessible.

I. INTRODUCTION

In recent years, the Internet of Things (IoT) has attracted much attention, and is expected to support different applications such as smart homes, smart gateways, environmental monitoring, and smart cities [1], [2]. Different from human-type communications, the IoT spawns a new communication scenario named massive connectivity, where a huge number of devices can access a single base station (BS) in a sporadic manner. In this scenario, the conventional grant-based random access solutions designed for human-type communications becomes very inefficient due to severe latency caused by device collisions [3].

Grant-free non-orthogonal random access (GF-NORA) has been considered as a promising technique for massive connectivity [3], [4], where active devices are allowed to directly transmit pilots and data to the BS without waiting for a grant. As such, in each transmission frame, the BS needs to conduct device activity detection (DAD), channel estimation (CE), and data detection (DD). A possible solution to this problem is to divide each transmission frame into a pilot phase and a data phase. The pilot phase is for pilot transmission at the devices and joint DAD and CE at the BS, and the data phase is for data transmission at the devices and DD at the BS. Since the device activity patterns are sporadic, at any given time, only a small and random fraction of all devices are active. Joint DAD and CE can be cast into a compressed sensing (CS) problem, where advanced compressed sensing algorithms, such as approximate message passing (AMP) [5], sparse Bayesian learning (SBL) [6], turbo compressed sensing (Turbo-CS) [7], and variance state propagation (VSP) [8], can be used to solve the problem. For example, the authors in [9] formulated the joint DAD and CE problem as a compressed sensing multiple measurement vector (MMV) problem by assuming multiple receive antennas, and used the AMP algorithm to solve the formulated problem. In [10], the turbo generalized MMV (GMMV) algorithm was proposed to solve the joint DAD and CE problem in a MIMO system with mixed analog-to-digital converters. In addition to user sparsity, the channel sparsity in the angle domain of the receiver antenna array can also help with joint DAD and CE. For example, [11] exploited user-angle-domain sparsity in a massive MIMO grant-free system and proposed a Turbo-GMMV-AMP algorithm for the problem. Moreover, machine learning technologies have been applied to further improve the performance. In [12], the authors used a deep neural network to learn the weights involved in message passing to improve the convergence performance. In contrast to the two-phase approach, another line of research proposed an one-phase approach [13], [14], where

the BS is required to conduct joint DAD, CE and DD. As compared to the two-phase approach, the more challenging one-phase approach generally increases the computational complexity, but can achieve significant performance improvement by efficiently exploiting the structure (such as sparsity and low rank) inherent in the channels and the signals.

Due to the limited coverage of terrestrial BSs, the development of terrestrial IoT is highly restricted in extreme environments such as deserts, forests, and oceans. Recently, satellite is considered as a potential solution for global IoT services [15]–[17]. In particular, low earth orbit (LEO) satellites supplement and extend terrestrial IoT systems, which can effectively solve the environmental constraints faced by terrestrial networks. In addition, the LEO satellite-IoT system has the ability to be immune to natural disasters and to guarantee all-weather communication. Compared with geostationary orbit (GEO) satellites, LEO satellites operate in low-earth orbits with a height typically lower than 2000 km. A shorter communication distance provides a more real-time IoT service. Yet, the LEO satellite raises new features due to the high speed and the long distance between satellites and ground devices:

- Large transmission delay: The delay of LEO satellite channel¹, though much shorter than that of a GEO satellite, is typically more than 1 ms, and is still quite large compared with that in terrestrial networks. Ref. [18] and Ref. [19] proposed to use global navigation satellite system (GNSS) based techniques to synchronize the devices and the satellite, and the delay of each device can be largely compensated. The residual delay can be handled by existing techniques such as the use of cyclic prefix (CP) in the orthogonal frequency division multiplexing (OFDM) system.
- Severe Doppler effect: It has been reported in [20] that in a LEO satellite communication system with a carrier frequency of Ku band, the maximum Doppler shift can be over 200 kHz. In [21], the authors considered GF-NORA in LEO satellite-IoT, and assumed that with the help of terrestrial BSs, the Doppler shifts are completely compensated. But this method is not applicable in remote areas without terrestrial BS. In addition, with GNSS, the devices can acquire their position information and calculate the Doppler shifts. However, the compensation of the Doppler shifts at the terrestrial device is incomplete, since there are typically more than one path and a terrestrial device can only compensate the Doppler shift of one path. The residual Doppler shifts of Ku-band signals can be over several thousand

¹The delay refers to the transmission time of the electromagnetic signals during the space between the device and the satellite.

Hertz. As such, it is of pressing interest to design a grant-free random access scheme that can reliably handle the severe Doppler effect of the LEO satellite-IoT channel.

In this paper, we assume that with the aid of GNSS, the device delays of the satellite channel can be largely compensated. Then we adopt the OFDM technique to deal with the residual delays, providing that the residual delays do not exceed the length of CP. Besides, since the Doppler shift compensation at the IoT devices is expensive and inaccurate, we propose to deal with the Doppler effect at the satellite by assuming that the average Doppler shift of the devices in a beam is estimated and then compensated. We focus on the joint DAD and CE problem in an GF-NORA for LEO satellite-IoT, where active devices suffer from the residual Doppler effect.

To distinguish the Doppler components with high precision, we adopt the OFDM-symbol repetition technique for the pilot design, where a super OFDM symbol are constructed by concatenating repeated regular OFDM symbols. In [22], [23], the authors designed the long preamble sequence by concatenating the circularly shifted replicas of a short Zadoff–Chu (ZC) sequence, for the random access in satellite communication. In addition, similar repetition techniques have been used for carrier frequency offset estimation for a single user, while the receiver carries out the maximum Likelihood (ML) estimation of the carrier frequency offset [24]–[27]. The problem considered in this paper is more challenging. On one hand, due to the multi-path effect, each IoT device generally has more than one Doppler component. On the other hand, there are a large number of devices in the satellite-IoT system. As such, the ML-based estimation methods, if applied directly, may incur a prohibitively high computational complexity.

To estimate the time-varying channel of satellite-IoT, we represent the channel with a grid-based parametric model, and point out that the time-varying OFDM channel exhibits block sparsity in the delay-Doppler domain. Then, together with the sparsity in the user domain (due to sporadic transmission of the terrestrial devices), we formulate the joint DAD and CE problem for OFDM-based GF-NORA in LEO satellite-IoT as a sparse signal recovery problem. Many existing compressed sensing algorithms [5]–[8], [28]–[31] can be applied to provide approximate solutions to the problem. It is known that Bayesian CS algorithms, such as AMP and Turbo-CS, can achieve significant performance improvement over non-Bayesian methods in sparse signal reconstruction. But AMP and Turbo-CS generally rely on a certain randomness property of the measurement matrix to ensure convergence, and the recovery performance of these algorithms may degrade seriously when such randomness is not met.

As inspired by the robustness of the VSP algorithm to a broad family of measurement matrices,

we extend the VSP algorithm to the massive connectivity scenario by appropriately handling the user sparsity prior, with the resulting algorithm termed modified VSP (MVSP). Specifically, we characterize the channel sparsity structure in the delay-Doppler-user domain with a probability model, which consists of a linear module and a Markov random field (MRF) module. The linear module handles the linear constraint between received signal and unknown vector, and the MRF module handles the block-sparse prior in the delay-Doppler domain as well as the sparse prior in the user domain. Different from the original Ising model [32] in the MRF, we introduce an auxiliary variable to characterize the relationship between the channel states and the device activity. The two modules are iterated until convergence. The proposed approach generally suffers from the energy leakage problem since the employed parametric channel model is based on a two-dimensional grid in the delay-Doppler domain. To reduce the mismatch between the actual channel and its on-grid representation, an expectation-maximization (EM) based learning method, named EM-MVSP, is proposed to update the delay-Doppler grid parameters. The contributions of this paper are summarised as follows.

- We develop a grid-based parametric system model for the OFDM-based satellite-IoT, and formulate the joint DAD and CE problem as a sparse signal recovery problem. Interestingly, we show that the measurement matrix in our considered problem can only be partially manipulated by the design of pilots, and exhibits a special correlation structure caused by the Doppler effect. Our experiments show that most existing compressed sensing algorithms including AMP and Turbo-CS behave poorly in the considered problem.
- To distinguish the Doppler components, we adopt the OFDM-symbol repetition technique to increase the frequency resolution of the OFDM system. We show that this OFDM-symbol repetition technique can efficiently improve the DAD and CE performance of the OFDM-based satellite-IoT system.
- We propose the MVSP algorithm for the joint DAD and CE problem, which is robust to the measurement matrix in our problem. Different from the original VSP algorithm, we introduce an auxiliary variable to characterize the relationship between the channel states and the device activity, and thus the DAD can be conducted by the MRF module.
- To alleviate the mismatch of the grid-base model, we further propose the EM-MVSP algorithm to update the grid parameters using EM method. We show that significant performance improvement can be achieved by the EM-MVSP algorithm, as compared to the counterpart

TABLE I
FREQUENTLY USED ABBREVIATIONS AND CORRESPONDING MEANING.

Abbr.	Meaning	Abbr.	Meaning
AMP	Approximate message passing	CE	Channel estimation
CP	Cyclic prefix	CS	Compressed sensing
DAD	Device activity detection	EM	Expectation–maximization
GAMP	Generalized approximate message passing	GF-NORA	Grant-free non-orthogonal random access
GNSS	Global navigation satellite system	IoT	Internet of Things
LEO	Low earth orbit	ML	Maximum Likelihood
MRF	Markov random field	MVSP	Modified variance state propagation
NMSE	Normalized mean-squared error	OFDM	Orthogonal frequency division multiplexing
OMP	Orthogonal matching pursuit	PCSBL	Pattern-coupled sparse Bayesian learning
SBL	Sparse Bayesian learning	SNR	Signal-noise-ratio
STCS	Structured turbo compressed sensing	VSP	Variance state propagation

algorithms including AMP, SBL, Turbo-CS and MVSP.

The rest of the paper is organized as follows. Section II introduces the time-varying satellite-IoT channel and the GF-NORA satellite-IoT system model, and then transforms it to a parametric form. Section III formulates the DAD and CE problem, constructs a probability model, and presents the MVSP algorithm. In Section IV, the MVSP algorithm is extended to the mismatch scenario with the EM framework. Numerical results are given in Section V, and Section VI concludes this paper. The frequently used abbreviations in this paper are summarized in Table I.

Notation: We use a bold symbol lowercase letter and bold symbol capital letter to denote a vector and a matrix, respectively. The trace, transpose, conjugate transpose, inverse, vectorization and Frobenius norm of a matrix are denoted by $\text{Tr}(\cdot)$, $(\cdot)^T$, $(\cdot)^H$, $(\cdot)^{-1}$, $\text{vec}(\cdot)$ and $\|\cdot\|_F$, respectively; \propto represents both sides of the equation are multiplicatively connected to a constant; $\text{diag}(\mathbf{a})$ forms a diagonal matrix with the diagonal elements in \mathbf{a} ; $|\cdot|$ denotes the modulus of a complex number; $\|\cdot\|$ denotes the ℓ^2 norm; $\mathbb{E}_p[\mathbf{x}]$ denotes the expectation of \mathbf{x} with respect to distribution p ; \otimes denotes the Kronecker product; $[N]$ denotes the set $\{1, 2, \dots, N\}$; $\delta(\cdot)$ denotes the Dirac delta function; The Gaussian and complex Gaussian distribution of \mathbf{x} with mean $\bar{\mathbf{m}}$ and covariance matrix Σ is denoted by $\mathcal{N}(\mathbf{x}; \bar{\mathbf{m}}, \Sigma)$ and $\mathcal{CN}(\mathbf{x}; \bar{\mathbf{m}}, \Sigma)$, respectively.

II. SYSTEM MODEL

A. Time-Varying Satellite-IoT Channel

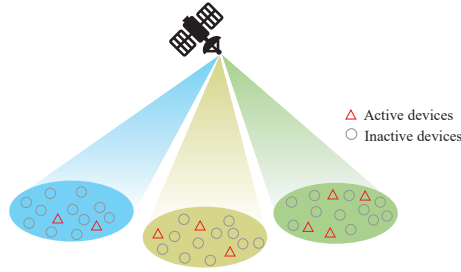


Fig. 1. The LEO satellite-IoT model.

As illustrated in Fig. 1, we consider a multi-beam LEO-satellite system where there exists K potential devices within a beam coverage. We assume that the signals in different beams are orthogonal, i.e., the inter-beam interference is ignored. Then, within a beam, the noiseless baseband received scalar signal from device k at the satellite can be expressed as

$$r_k(t) = \int_{-\infty}^{\infty} \int_{-\infty}^{\infty} \bar{h}_k(\tau, \nu) s_k(t - \tau) e^{j2\pi\nu t} d\tau d\nu, \quad (1)$$

where $\bar{h}_k(\tau, \nu)$ is the channel impulse response at delay τ and Doppler frequency ν , and $s_k(t)$ is the signal from the k -th device. As different devices are usually geographically separated, we assume that the channel realizations between the satellite and different devices are uncorrelated. We also assume that with the help of GNSS, the delay can be partially pre-compensated at the device, and the satellite uses the Doppler frequency shift at the beam center to compensate all the devices in the beam. As such, the impact of the transmission delay and Doppler frequency shift can be largely eliminated, or in other words, only the residual delay and the residual Doppler frequency shift need to be taken into account. Without loss of generality, we assume that there exist P_k paths for each device k , where P_k is a small positive integer since the satellite communication is typically in a weak multipath transmission environment. The residual delay and the residual Doppler shift of the p -th path of device k are denoted as $\bar{\tau}_{k,p}$ and $\bar{\nu}_{k,p}$, respectively. We assume that $\bar{\tau}_{k,p}$ and $\bar{\nu}_{k,p}$ are constant during a transmission frame. The corresponding attenuation including path loss, reflection and processing gains of each device in the p -th path is characterized by a complex coefficient $\bar{h}_{k,p}$. Therefore, $\bar{h}_k(\tau, \nu)$ can be approximated by

$$\bar{h}_k(\tau, \nu) = \sum_{p=0}^{P_k-1} \bar{h}_{k,p} \delta(\tau - \bar{\tau}_{k,p}) \delta(\nu - \bar{\nu}_{k,p}). \quad (2)$$

Substituting (2) into (1) yields

$$r_k(t) = \sum_{p=0}^{P_k-1} \bar{h}_{k,p} s_k(t - \bar{\tau}_{k,p}) e^{j2\pi\bar{\nu}_{k,p}t}. \quad (3)$$

B. Grant-Free Satellite-IoT System Model

In this paper, we adopt the grant-free non-orthogonal random access (GF-NORA) scheme, in which the devices share the physical channel resource and directly transmit their signals without requiring the permission of the satellite. Following [3], we assume that each transmission frame in GF-NORA consists of two phases, namely, the pilot phase and the data phase. Each device is preassigned with a unique non-orthogonal pilot sequence. In the pilot phase, the active devices transmit their pilots, based on which the satellite detects the active devices and estimates their channels. In the data phase, the devices transmit data without the grant from the satellite, and the satellite decodes the data based on the estimated channel of the active devices. Orthogonal frequency division multiplexing (OFDM) is employed for both the pilot and data transmission phases. In this work, we focus on the device activity detection (DAD) and channel estimation (CE) in the pilot phase. The system model of the pilot phase is described as follows.

In the pilot phase, we construct a super-symbol by concatenating N repetitions of an OFDM symbol, and a cyclic prefix (CP) is applied to eliminate the inter-symbol interference, as shown in Fig. 2. The duration of such a super-symbol with a CP is $\bar{T} = NT + T_{\text{cp}}$, where T is the length of a regular OFDM symbol, $T_{\text{cp}} > \tau_{\text{max}}$ is the length of the CP, and τ_{max} is the maximal residual delay for all devices. We note that the above repetitions of an OFDM symbol improve the frequency resolution of the receiver, so that the Doppler frequency shifts can be identified more clearly and thus its adverse effect can be more efficiently mitigated. Without loss of generality, we assume that the pilot sequence of a device contains U consecutive super-symbols. The frequency spacing between any two adjacent subcarriers is set to $\Delta f = 1/T$. In the u -th super-symbol, the baseband modulated signal at the k -th device is given by

$$d_{k,u}(t) = \sum_{m=0}^{M-1} x_{k,m,u} e^{j2\pi m \Delta f t} \xi(t - u\bar{T}), \forall k, \forall u, \quad (4a)$$

where $x_{k,m,u}$ is the pilot on the m -th subcarrier in the u -th super-symbol of the k -th device, and

$$\xi(t) = \begin{cases} 1, & t \in [-T_{\text{cp}}, NT], \\ 0, & \text{otherwise,} \end{cases} \quad (4b)$$

is the transmitted rectangular pulse. The baseband pilot signal of device k is given by

$$s_k(t) = \sum_{u=0}^{U-1} d_{k,u}(t), \forall k, \quad (4c)$$

where U is the number of super-symbols in a pilot sequence.

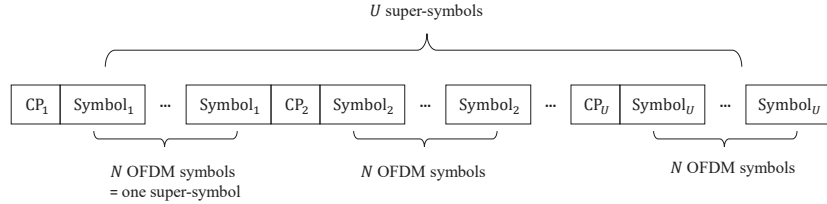


Fig. 2. The structure of a pilot sequence in the pilot phase.

In each transmission frame, only a small subset of devices are active. To characterize such sporadic transmission, the device activity is represented by an indicator function α_k as

$$\alpha_k = \begin{cases} 1, & \text{if device } k \text{ is active,} \\ 0, & \text{if device } k \text{ is inactive,} \end{cases} \quad k = 1, \dots, K, \quad (5)$$

with a probability $p(\alpha_k = 1) = \rho$ where $\rho \ll 1$. Combining (3), (4a), (4c) and (5), the received baseband signal of all devices at the satellite can be expressed as

$$\begin{aligned} r(t) &= \sum_{k=1}^K r_k(t) + w(t) \\ &= \sum_{k=1}^K \alpha_k \sum_{p=0}^{P_k-1} e^{j2\pi\bar{\nu}_{k,p}t} \bar{h}_{k,p} \sum_{u=0}^{U-1} \sum_{m=0}^{M-1} x_{k,m,u} e^{j2\pi m\Delta f(t-\bar{\tau}_{k,p})} \xi(t - \bar{\tau}_{k,p} - u\bar{T}) + w(t), \end{aligned} \quad (6)$$

where $w(t)$ is an additive white Gaussian noise (AWGN).

In a conventional OFDM system with symbol duration T , any two subcarriers with minimum frequency shift $\Delta f = 1/T$ are orthogonal to each other, i.e., the frequency resolution is the subcarrier spacing $1/T$. In our super-symbol system, since each super-symbol consists of N repeated regular OFDM symbols, the frequency resolution is $1/(NT)$. In other words, N -time oversampling in the frequency domain can be applied in our system. In the u -th super-symbol interval, the demodulated signals with N -time oversampling is given by

$$y_{n,u} = \frac{1}{NT} \int_{u\bar{T}}^{u\bar{T}+NT} r(t) e^{-j2\pi\frac{n}{N}\Delta ft} dt, \quad \text{for } n \in \{0, 1, \dots, NM - 1\}, \quad (7)$$

where the boundary of the observation window of the u -th super-symbol specifies the upper and lower limits of the integral. By plugging (6) into (7), $y_{n,u}$ can be expressed as

$$\begin{aligned} y_{n,u} &= \sum_{k=1}^K \frac{\alpha_k}{NT} \sum_{m=0}^{M-1} x_{k,m,u} \sum_{p=0}^{P_k-1} e^{-j2\pi m \Delta f \bar{\tau}_{k,p}} \bar{h}_{k,p} \int_{u\bar{T}}^{u\bar{T}+NT} e^{j2\pi \bar{\nu}_{k,p} t} e^{j2\pi(m-\frac{n}{N})\Delta f t} dt + w_{n,u} \\ &= \sum_{m=0}^{M-1} \sum_{k=1}^K x_{k,m,u} g_{m,n,k,u} + w_{n,u}, \end{aligned} \quad (8a)$$

where $w_{n,u} = \int_{u\bar{T}}^{u\bar{T}+NT} e^{j2\pi \frac{n}{N} \Delta f t} w(t) dt$, and

$$g_{m,n,k,u} = \frac{\alpha_k}{NT} \sum_{p=0}^{P_k-1} e^{-j2\pi m \Delta f \bar{\tau}_{k,p}} \bar{h}_{k,p} \int_{u\bar{T}}^{u\bar{T}+NT} e^{j2\pi \bar{\nu}_{k,p} t} e^{j2\pi(m-\frac{n}{N})\Delta f t} dt. \quad (8b)$$

Let $\mathbf{x}_{m,u} = [x_{1,m,u}, \dots, x_{K,m,u}]^T$ and $\mathbf{g}_{m,n,u} = [g_{m,n,1,u}, \dots, g_{m,n,K,u}]^T$. We can rewrite $y_{n,u}$ as

$$y_{n,u} = \sum_{m=0}^{M-1} \mathbf{x}_{m,u}^T \mathbf{g}_{m,n,u} + w_{n,u}. \quad (9)$$

Let $\mathbf{y}_u = [y_{0,u}, \dots, y_{NM-1,u}]^T$. We have

$$\mathbf{y}_u = \mathbf{G}_u \mathbf{x}_u + \mathbf{w}_u, \quad (10a)$$

where $\mathbf{w}_u = [w_{0,u}, \dots, w_{NM-1,u}]^T$ is the AWGN with variance σ^2 , $\mathbf{x}_u \triangleq [\mathbf{x}_{0,u}^T, \dots, \mathbf{x}_{M-1,u}^T]^T \in \mathbb{C}^{MK \times 1}$, and

$$\mathbf{G}_u \triangleq \begin{bmatrix} \mathbf{g}_{0,0,u}^T & \cdots & \mathbf{g}_{M-1,0,u}^T \\ \vdots & & \vdots \\ \mathbf{g}_{0,NM-1,u}^T & \cdots & \mathbf{g}_{M-1,NM-1,u}^T \end{bmatrix} \in \mathbb{C}^{NM \times MK}. \quad (10b)$$

\mathbf{G}_u characterizes the channels of all the M subcarriers in the u -th super-symbol. Our goal is to estimate $\{\mathbf{G}_u\}_{u=0}^{U-1}$ based on $\{\mathbf{y}_u\}_{u=0}^{U-1}$ and $\{\mathbf{x}_u\}_{u=0}^{U-1}$. A brute-force approach to this problem is infeasible since the number of observations in $\{\mathbf{y}_u\}_{u=0}^{U-1}$ is only UMK , which is far less than that of the unknown variables in $\{\mathbf{G}_u\}_{u=0}^{U-1}$, i.e., UNM^2K . As such, we need a more elegant representation of $\{\mathbf{G}_u\}_{u=0}^{U-1}$ with less unknowns, as detailed in the next subsection.

C. Grid-Based Parametric System Model

We now present a grid-based parametric model for the channel \mathbf{G}_u . From (8b) and (10b), the unknown parameters in \mathbf{G}_u include each device's path delays $\{\bar{\tau}_{k,p}\}_{p=0}^{P_k-1}$, path Doppler shifts $\{\bar{\nu}_{k,p}\}_{p=0}^{P_k-1}$ and channel gains $\{\bar{h}_{k,p}\}_{p=0}^{P_k-1}$. In practical wireless communication scenarios, each

channel path may consist of many sub-paths, and the parameters of all these sub-paths are usually difficult to distinguish. Exact identification of these parameters is therefore very challenging.

To address this issue, we discretize the delay domain and the Doppler domain into a two-dimensional grid. Instead of estimating the equivalent channel matrix \mathbf{G}_u , we estimate the representation of the channel on the grid. Then \mathbf{G}_u can be recovered based on the grid parameters and the corresponding channel representation. This approach avoids the estimation of each physical path or sub-path separately, but considers the overall representation of the physical channel on the delay-Doppler grid. In specific, for each device k , the grid parameters of the delay domain and the Doppler domain are defined as

$$\begin{aligned}\boldsymbol{\tau}_k &= \{\tau_{l,k}\}_{l=0}^{L-1}, \quad \tau_{l,k} \in [0, \tau_{\max}), \\ \boldsymbol{\nu}_k &= \{\nu_{j,k}\}_{j=0}^{J-1}, \quad \nu_{j,k} \in [-\nu_{\max}/2, \nu_{\max}/2).\end{aligned}$$

As such, the channel $\bar{h}_k(\tau, \nu)$ can be approximated as

$$\bar{h}_k(\tau, \nu) = \sum_{l=0}^{L-1} \sum_{j=0}^{J-1} h_{k,l,j} \delta(\tau - \tau_{k,l}) \delta(\nu - \nu_{k,j}), \quad (11)$$

where $h_{k,l,j}$ is device k 's channel representation at grid $(\tau_{k,l}, \nu_{k,j})$. We rewrite $y_{n,u}$ in (8a) as

$$\begin{aligned}y_{n,u} &= \frac{1}{NT} \int_{u\bar{T}}^{u\bar{T}+NT} r(t) e^{-j2\pi \frac{n}{N} \Delta f t} dt \\ &= \sum_{k=1}^K \frac{\alpha_k}{NT} \sum_{m=0}^{M-1} x_{k,m,u} \sum_{j=0}^{J-1} \int_{u\bar{T}}^{u\bar{T}+NT} e^{j2\pi \nu_{k,j} t} e^{j2\pi(m-\frac{n}{N})\Delta f t} dt \sum_{l=0}^{L-1} e^{-j2\pi m \Delta f \tau_{k,l}} h_{k,l,j} + w_{n,u}. \quad (12)\end{aligned}$$

Let $\mathbf{b}_{k,m} = [e^{-j2\pi m \Delta f \tau_{k,0}}, \dots, e^{-j2\pi m \Delta f \tau_{k,L-1}}]^T \in \mathbb{C}^{L \times 1}$, $\mathbf{h}_{k,j} = [h_{k,0,j}, \dots, h_{k,L-1,j}]^T \in \mathbb{C}^{L \times 1}$, and $c_{k,m,n,j,u} = \frac{1}{NT} \int_{u\bar{T}}^{u\bar{T}+NT} e^{j2\pi \nu_{k,j} t} e^{j2\pi(m-\frac{n}{N})\Delta f t} dt$. We rewrite (12) as

$$\begin{aligned}y_{n,u} &= \sum_{k=1}^K \alpha_k \sum_{m=0}^{M-1} x_{k,m,u} \sum_{j=0}^{J-1} c_{k,m,n,j,u} \mathbf{b}_{k,m}^T \mathbf{h}_{k,j} + w_{n,u} \\ &= \sum_{k=1}^K \alpha_k \left[\sum_{m=0}^{M-1} x_{k,m,u} (\mathbf{b}_{k,m}^T \otimes \mathbf{c}_{k,m,n,u}^T) \right] \text{vec}(\mathbf{H}_k^T) + w_{n,u} \\ &= \sum_{k=1}^K \alpha_k \mathbf{a}_{k,n,u} \text{vec}(\mathbf{H}_k^T) + w_{n,u}, \quad (13a)\end{aligned}$$

where $\mathbf{c}_{k,m,n,u} = [c_{k,m,n,0,u}, \dots, c_{k,m,n,J-1,u}]^T \in \mathbb{C}^{J \times 1}$, $\mathbf{H}_k = [\mathbf{h}_{k,0}, \dots, \mathbf{h}_{k,J-1}] \in \mathbb{C}^{L \times J}$, and

$$\mathbf{a}_{k,n,u} = \sum_{m=0}^{M-1} x_{k,m,u} (\mathbf{b}_{k,m}^T \otimes \mathbf{c}_{k,m,n,u}^T) \in \mathbb{C}^{1 \times LJ}. \quad (13b)$$

Then we have

$$\mathbf{y}_u = \mathbf{A}_u \mathbf{h} + \mathbf{w}_u, \quad (14a)$$

where $\mathbf{h}_u \triangleq [\alpha_1 \text{vec}(\mathbf{H}_1^T)^T, \dots, \alpha_K \text{vec}(\mathbf{H}_K^T)^T]^T \in \mathbb{C}^{Q \times 1}$,

$$\mathbf{A}_u \triangleq \begin{bmatrix} \mathbf{a}_{1,0,u} & \cdots & \mathbf{a}_{K,0,u} \\ \vdots & & \\ \mathbf{a}_{1,NM-1,u} & \cdots & \mathbf{a}_{K,NM-1,u} \end{bmatrix} \in \mathbb{C}^{NM \times Q}, \quad (14b)$$

$R = NMU$ and $Q = KLJ$. \mathbf{h} combines the device activity and delay-Doppler grid parameters. Note that \mathbf{h} is a sparse vector since the channel is sparse in the user-delay-Doppler domain, as elaborated in Section II-D.

Denote by $\mathbf{y} \triangleq [\mathbf{y}_0^T, \dots, \mathbf{y}_{U-1}^T]^T \in \mathbb{C}^{R \times 1}$ the collection of all the U demodulated super-symbols in the pilot phase. From (14a), we obtain

$$\mathbf{y} = \mathbf{A} \mathbf{h} + \mathbf{w}, \quad (15)$$

where $\mathbf{A} = [\mathbf{A}_0^T, \dots, \mathbf{A}_{U-1}^T]^T \in \mathbb{C}^{R \times Q}$, and $\mathbf{w} = [\mathbf{w}_0^T, \dots, \mathbf{w}_{U-1}^T]^T \in \mathbb{C}^{R \times 1}$.

We emphasize that \mathbf{h} contains all the unknown channel parameters for the reconstruction of the channels $\{\mathbf{G}_u\}_{u=0}^{U-1}$. To be specific, we use model (10a) to generate channels and signals in simulation, and use the discretized model (15) to design DAD and CE algorithms. We then reconstruct the channel \mathbf{G}_u by the estimated \mathbf{h} . Suppose that $\hat{\mathbf{h}}$ is an estimate of \mathbf{h} , $\hat{h}_{k,l,j}$ is the estimate corresponding to the (k, l, j) grid point, and $\hat{\alpha}_k$ is an estimate of α_k . Then the recovered channel is given by

$$\hat{\mathbf{G}}_u \triangleq \begin{bmatrix} \hat{\mathbf{g}}_{0,0,u}^T & \cdots & \hat{\mathbf{g}}_{M-1,0,u}^T \\ \vdots & & \\ \hat{\mathbf{g}}_{0,NM-1,u}^T & \cdots & \hat{\mathbf{g}}_{M-1,NM-1,u}^T \end{bmatrix}, \quad (16a)$$

where $\hat{\mathbf{g}}_{m,n,u} = [\hat{g}_{m,n,1,u}, \hat{g}_{m,n,2,u}, \dots, \hat{g}_{m,n,K,u}]^T$, and

$$\hat{g}_{m,n,k,u} = \frac{\hat{\alpha}_k}{NT} \sum_{l=0}^{L-1} \sum_{j=0}^{J-1} e^{-j2\pi m \Delta f \tau_{k,l}} \hat{h}_{k,l,j} \int_{u\bar{T}}^{u\bar{T}+NT} e^{j2\pi \nu_{k,j} t} e^{j2\pi(m-\frac{n}{N})\Delta f t} dt. \quad (16b)$$

The normalized mean-squared error (NMSE) of the channel estimation is defined by

$$\text{NMSE} = \frac{1}{U} \sum_{u=0}^{U-1} \frac{\mathbb{E} [\|\hat{\mathbf{G}}_u - \mathbf{G}_u\|_{\text{F}}^2]}{\mathbb{E} [\|\mathbf{G}_u\|_{\text{F}}^2]}. \quad (17)$$

D. Channel Sparsity

It is well known that channel sparsity can be exploited to significantly reduce the number of pilots required in channel estimation. In this regard, the channel in our considered satellite-IoT scenario exhibit the following sparsity structure:

- 1) Sparsity in the user domain: Most of the devices are inactive at any given time, i.e., most of $\{\alpha_k\}$ are zero.
- 2) Sparsity in the delay-Doppler domain: Since the satellite communication is in a weak multi-path transmission environment, the numbers of dominant paths between the satellite and the devices are limited.
- 3) Block-sparsity in the delay-Doppler domain: The scattering effect of the electromagnetic waves causes delay and Doppler spread in wireless channels. Besides, the grid mismatch causes additional spreading in the delay-Doppler domain. These effects make the channel coefficients appear in clusters in the delay-Doppler domain.

Fig. 3 illustrates the sparsity structure of \mathbf{h} in the delay-Doppler-user domain. This sparsity structure is exploited in the design of the receiver.

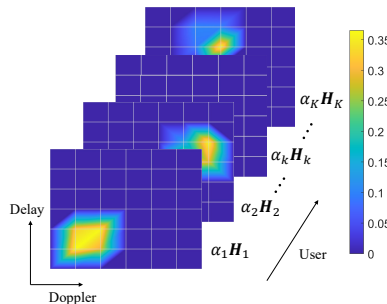


Fig. 3. An illustration of the channel sparsity structure.

E. Problem Description

Recall that the receiver of the considered grant-free satellite-IoT system carries out joint DAD and CE. With (15) and the discussions in Subsection D, the joint DAD and CE problem is to estimate a sparse vector \mathbf{h} given the observation \mathbf{y} . Various compressed sensing algorithms have been proposed to solve the linear-inverse problem in the form of (15). However, popular Bayesian algorithms, such as AMP and Turbo-CS, suffer from significant performance degradation when applied to our problem. This is because AMP and Turbo-CS generally rely on the randomness

of the measurement matrix \mathbf{A} to ensure convergence. For example, the recovery performance of AMP is guaranteed only when the elements of \mathbf{A} are independently and identically distributed (i.i.d.) Gaussian; as for Turbo-CS, \mathbf{A} is required to be right-rotationally invariant. When the randomness requirement of \mathbf{A} is not met, the recovery performance of the corresponding algorithms will be seriously degraded. In this work, the structure of \mathbf{A} cannot be arbitrarily designed. From (13b) and (14b), each row of \mathbf{A} is the sum of a series of Kronecker products. This introduces correlation between the elements in a same row of \mathbf{A} . Fig. 4(a) shows the local thermogram of \mathbf{A} in a random experiment, which reflects the amplitude of the elements in \mathbf{A} . It is clear that the amplitudes of the elements in a same row are correlated, rather than independent and identically distributed. As a comparison, Fig. 4(b) shows the thermogram of a matrix of the same size with each element randomly drawn from the standard complex Gaussian distribution. Fig. 4(c) shows the local thermogram of $\mathbf{A}\mathbf{F}$ where \mathbf{F} is a discrete Fourier transform (DFT) matrix (which is unitary). Clearly, $\mathbf{A}\mathbf{F}$ and \mathbf{A} show different patterns. Therefore \mathbf{A} is not a right-rotationally invariant matrix, and thus does not meet the randomness requirements of both AMP and Turbo-CS. We will see that AMP and Turbo-CS perform poorly for this task in simulations.

Considering the special structure of \mathbf{A} in (15), we follow the variance state propagation (VSP) framework proposed in [8] and propose the MVSP algorithm to solve this sparse signal recovery problem. Compared with AMP and Turbo-CS, the MVSP algorithm is more robust to the structure of the measurement matrix, which is derived in next section.

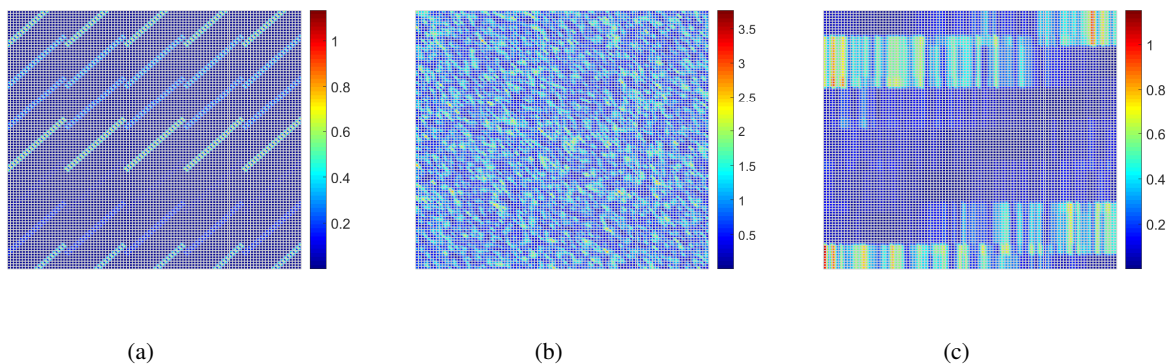


Fig. 4. Thermograms of random matrices. (a) local (the first 100 rows and the first 100 columns) thermogram of \mathbf{A} in (15) in a random experiment. (b) Thermogram of a matrix with each entry randomly drawn from a standard complex Gaussian distribution. (c) local (the first 100 rows and the first 100 columns) thermogram of $\mathbf{A}\mathbf{F}$ where \mathbf{F} is a unitary DFT matrix.

III. RECEIVER DESIGN FOR JOINT DAD AND CE

In this section, we first introduce the probability model and the problem formulation, and then derive the MVSP algorithm based on a factor-graph representation of the probability model.

A. Probability Model

For notational convenience, we rewrite \mathbf{h} as

$$\mathbf{h} = [h_{1,1}, h_{1,2}, \dots, h_{1,LJ}, \dots, h_{K,1}, h_{K,2}, \dots, h_{K,LJ}]^T.$$

Similarly to [33], we assign the sparse channel \mathbf{h} with a conditional Gaussian prior as

$$p(\mathbf{h}|\mathbf{v}) = \prod_{k=1}^K \prod_{i=1}^{LJ} p(h_{k,i}|v_{k,i}), \quad (18)$$

where $\mathbf{v} = [v_{1,1}, v_{1,2}, \dots, v_{K,LJ}]$, and $p(h_{k,i}|v_{k,i}) = \mathcal{CN}(h_{k,i}; 0, v_{k,i})$ is a circularly symmetric complex Gaussian (CSCG) distribution with zero mean and variance $v_{k,i}$, $k \in \{1, \dots, K\}$, $i \in \{1, \dots, LJ\}$. Each $v_{k,i}$ is assigned with a conditionally independent distribution given by

$$p(v_{k,i}|s_{k,i}) = \text{Gamma}(v_{k,i}; \gamma_{k,1}, \gamma_{k,2}) \delta(s_{k,i} - 1) + \delta(v_{k,i}) \delta(s_{k,i} + 1), \quad (19)$$

where $s_{k,i} \in \{-1, 1\}$ is a hidden binary state; $\text{Gamma}(v_{k,i}; \gamma_{k,1}, \gamma_{k,2})$ is the Gamma distribution

$$\text{Gamma}(v_{k,i}; \gamma_{k,1}, \gamma_{k,2}) = \begin{cases} \frac{\gamma_{k,1}^{\gamma_{k,1}} v_{k,i}^{\gamma_{k,1}-1} e^{-\gamma_{k,2} v_{k,i}}}{\Gamma(\gamma_{k,1})}, & v_{k,i} > 0, \\ 0, & \text{otherwise,} \end{cases} \quad (20)$$

with $\Gamma(\gamma_{k,1}) = \int_0^\infty t^{\gamma_{k,1}-1} e^{-t} dt$ being the Gamma function.

Then, a Markov random field (MRF) prior is used to characterize the sparse structure of \mathbf{v} . The joint probability of the hidden state and device activity variables is modeled as

$$p(\mathbf{s}_k, \alpha_k) \propto \prod_{i=1}^{LJ} \prod_{z \in \mathcal{D}_i} (\varphi(s_{k,z}, s_{k,i}))^{\frac{1}{2}} \psi(\ell_k, \alpha_k) p(\alpha_k), \quad (21)$$

where $\mathbf{s}_k = [s_{k,1}, s_{k,2}, \dots, s_{k,LJ}]$, $\varphi(s_{k,z}, s_{k,i}) = \exp(\beta s_{k,z} s_{k,i})$, and $\ell_k = \sum_i^{LJ} s_{k,i}$; \mathcal{D}_i denotes the set includes the indexes of the left, right, top and bottom neighbors of $s_{k,i}$, i.e., $\{i-1, i+1, i-J, i+J\}$; β is the parameter of the MRF, corresponding to the average size of non-zero blocks. Different from the original Ising model [32], we add the constraint $\psi(\ell_k, \alpha_k)$ that represents the conditional probability density of ℓ_k given α_k . Note that ℓ_k is discrete since each $s_{k,i}$ is binary.

However, since LJ is large, ℓ_k for an active device k (i.e., $\alpha_k = 1$) can be well approximated by a Gaussian random variable. Thus, we have

$$\psi(\ell_k, \alpha_k) = \mathcal{N}(\ell_k; m_\psi, \sigma_\psi^2) \delta(\alpha_k - 1) + \delta(\ell_k + 1) \delta(\alpha_k), \quad (22a)$$

where m_ψ and σ_ψ^2 are the mean and variance of ℓ_k conditioned on $\alpha_k = 1$, respectively given by $m_\psi = LJ(2\rho_s - 1)$ and $\sigma_\psi^2 = 4LJ\rho_s(1 - \rho_s)$, and ρ_s is the sparsity rate of $\{v_{k,i}\}_{i=1}^{LJ}$, i.e., $p(s_{k,i} = 1) = \rho_s$. The joint probability of $p(\mathbf{y}, \mathbf{h}, \mathbf{v}, \mathbf{s}, \boldsymbol{\alpha})$ can be decomposed as

$$\begin{aligned} p(\mathbf{y}, \mathbf{h}, \mathbf{v}, \mathbf{s}, \boldsymbol{\alpha}) &= p(\mathbf{y}|\mathbf{h}) p(\mathbf{h}|\mathbf{v}) p(\mathbf{v}|\mathbf{s}) p(\mathbf{s}, \boldsymbol{\alpha}) \\ &= p(\mathbf{y}|\mathbf{h}) \prod_{k=1}^K \prod_{i=1}^{LJ} p(h_{k,i}|v_{k,i}) p(v_{k,i}|s_{k,i}) \prod_{k=1}^K p(\mathbf{s}_k, \alpha_k), \end{aligned} \quad (23)$$

where $\mathbf{s} = [s_1, \dots, s_K]$ and $\boldsymbol{\alpha} = [\alpha_1, \dots, \alpha_K]$. The dependencies of the random variables in the factorization (23) can be shown by a factor graph as depicted in Fig. 5, where circles represent variable nodes and squares represent factor nodes. The factor nodes in Fig. 5 are defined as

$$\zeta_{k,i} : p(v_{k,i}|s_{k,i}), \quad (24a)$$

$$\eta_{k,i} : p(h_{k,i}|v_{k,i}) = \mathcal{CN}(h_{k,i}; 0, v_{k,i}), \quad (24b)$$

$$\iota : p(\mathbf{y}|\mathbf{h}) = \mathcal{CN}(\mathbf{y} - \mathbf{A}\mathbf{x}; \mathbf{0}, \sigma^2\mathbf{I}), \quad (24c)$$

$$\chi_k : \delta\left(\ell_k - \sum_i s_{k,i}\right), \quad (24d)$$

$$\psi_k : \psi(\ell_k, \alpha_k). \quad (24e)$$

The factor graph in Fig. 5 includes two modules, namely, the linear module that handles the linear constraint in (15) and the MRF module that handles the MRF prior in (21).

B. MVSP Algorithm

The MVSP algorithm is a sum-product message passing algorithm defined on Fig. 5. A major difference between MVSP and the original VSP in [8] is that variable nodes $\{\ell_k\}$ and $\{\alpha_k\}$ are added to the factor graph for device activity detection, which involves more sophisticated message updates in the MRF module. The details of the MVSP are presented in the following.

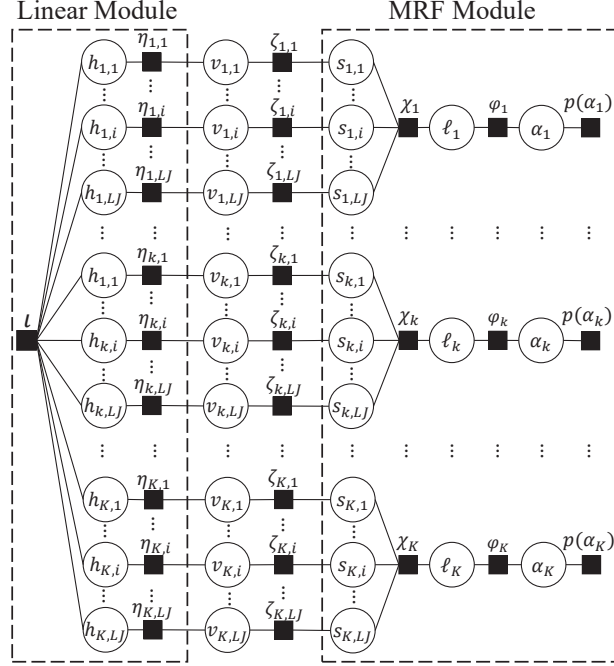


Fig. 5. The factor graph characterizing the hierarchical probability model for sparse signals.

Let $\varpi_{a \rightarrow b}$ denote the message passing from node a to node b . In Fig. 5, node $v_{k,i}$ receives a message $\varpi_{\eta_{k,i} \rightarrow v_{k,i}}$ from node $\eta_{k,i}$. From the sum-product rule, the message from $v_{k,i}$ to $\zeta_{k,i}$ is still given by $\varpi_{\eta_{k,i} \rightarrow v_{k,i}}$. Then the message from $\zeta_{k,i}$ to $s_{k,i}$ is a Bernoulli distribution given by

$$\varpi_{\zeta_{k,i} \rightarrow s_{k,i}} \propto \int_{v_{k,i}} p(v_{k,i} | s_{k,i}) \varpi_{\eta_{k,i} \rightarrow v_{k,i}} = \pi_{\zeta_{k,i} \rightarrow s_{k,i}} \delta(s_{k,i} - 1) + (1 - \pi_{\zeta_{k,i} \rightarrow s_{k,i}}) \delta(s_{k,i} + 1), \quad (25)$$

where $\pi_{\zeta_{k,i} \rightarrow s_{k,i}}$ is the probability of $s_{k,i} = 1$ specified in the message $\varpi_{\zeta_{k,i} \rightarrow s_{k,i}}$.

We now describe the message passing involved in the MRF (21). A 4-connected MRF is used in MVSP to leverage the block sparsity of each s_k in the delay-Doppler domain. The detailed factor graph characterizing the 4-connected MRF module is given in Fig. 6. For clarity, the left, right, top, bottom neighbors to $s_{k,i}$ are reindexed by $\mathcal{I}_i = \{i_L, i_R, i_T, i_B\}$ (i.e., $s_{k,i_L} = s_{k,i-1}$, $s_{k,i_R} = s_{k,i+1}$, $s_{k,i_T} = s_{k,i+J}$, $s_{k,i_B} = s_{k,i-J}$). The left, right, top, and bottom incoming messages of $s_{k,i}$, denoted as $\varpi_{k,i}^L$, $\varpi_{k,i}^R$, $\varpi_{k,i}^T$, and $\varpi_{k,i}^B$, are Bernoulli distributions. By defining $\mathcal{J} = \{L, R, T, B\}$, the incoming message of $s_{k,i}$ from the left is given by

$$\begin{aligned} \varpi_{k,i}^L &\propto \int_{s_{k,i_L}} \varpi_{\zeta_{k,i_L} \rightarrow s_{k,i_L}} \prod_{j \in \mathcal{J} \setminus R} \varpi_{k,i_L}^j \varphi(s_{k,i}, s_{k,i_L}) \varpi_{\chi_k \rightarrow s_{k,i_L}} \\ &= \lambda_{k,i}^L \delta(s_{k,i} - 1) + (1 - \lambda_{k,i}^L) \delta(s_{k,i} + 1), \end{aligned} \quad (26a)$$

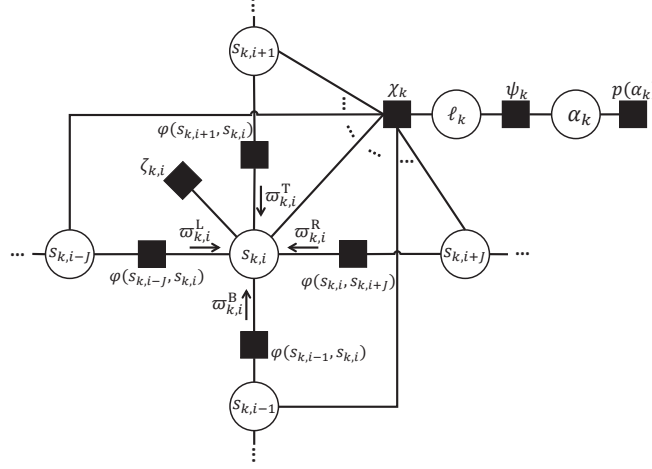


Fig. 6. Illustration of the MRF module in MVSP.

where $\mathcal{J} \setminus \text{R}$ denotes the set \mathcal{J} by excluding the element “R”, $\varpi_{\chi_k \rightarrow s_{k,i_L}}$ is the message from χ_k to s_{k,i_L} , denoted as

$$\varpi_{\chi_k \rightarrow s_{k,i_L}} = \pi_{\chi_k \rightarrow s_{k,i_L}} \delta(s_{k,i_L} - 1) + (1 - \pi_{\chi_k \rightarrow s_{k,i_L}}) \delta(s_{k,i_L} + 1), \quad (26b)$$

and $\lambda_{k,i}^L$ is given by (27).

The incoming messages of $s_{k,i}$ from the right, top, and bottom, i.e., $\varpi_{k,i}^R$, $\varpi_{k,i}^T$, and $\varpi_{k,i}^B$, have a form similar to $\varpi_{k,i}^L$. The message from χ_k to ℓ_k is expressed as

$$\varpi_{\chi_k \rightarrow \ell_k} \propto \int_{\mathbf{s}_k} \delta\left(\ell_k - \sum_i s_{k,i}\right) \prod_i \left(\varpi_{\zeta_{k,i} \rightarrow s_{k,i}} \prod_{j \in \mathcal{J}} \varpi_{k,i}^j\right). \quad (28)$$

Similarly to (22a), we approximate (28) with a Gaussian distribution:

$$\varpi_{\chi_k \rightarrow \ell_k} = \mathcal{N}(\ell_k; m_{\chi_k \rightarrow \ell_k}, \sigma_{\chi_k \rightarrow \ell_k}^2), \quad (29a)$$

$$\lambda_{k,i}^L = \frac{e^\beta \pi_{\zeta_{k,i_L} \rightarrow s_{k,i_L}} \pi_{\chi_k \rightarrow s_{k,i_L}} \prod_{j \in \mathcal{J} \setminus \text{R}} \lambda_{k,i_L}^j + e^{-\beta} (1 - \pi_{\zeta_{k,i_L} \rightarrow s_{k,i_L}}) (1 - \pi_{\chi_k \rightarrow s_{k,i_L}}) \prod_{j \in \mathcal{J} \setminus \text{R}} (1 - \lambda_{k,i_L}^j)}{(e^\beta + e^{-\beta}) \left(\pi_{\zeta_{k,i_L} \rightarrow s_{k,i_L}} \pi_{\chi_k \rightarrow s_{k,i_L}} \prod_{j \in \mathcal{J} \setminus \text{R}} \lambda_{k,i_L}^j + (1 - \pi_{\zeta_{k,i_L} \rightarrow s_{k,i_L}}) (1 - \pi_{\chi_k \rightarrow s_{k,i_L}}) \prod_{j \in \mathcal{J} \setminus \text{R}} (1 - \lambda_{k,i_L}^j) \right)} \quad (27)$$

where $m_{\chi_k \rightarrow \ell_k}$ and $\sigma_{\chi_k \rightarrow \ell_k}^2$ are the mean and variance, respectively given by $m_{\chi_k \rightarrow \ell_k} = \sum_i (2\pi_{s_{k,i} \rightarrow \chi_k} - 1)$ and $\sigma_{\chi_k \rightarrow \ell_k}^2 = 4 \sum_i \pi_{s_{k,i}} (1 - \pi_{s_{k,i}})$, and

$$\pi_{s_{k,i} \rightarrow \chi_k} = \frac{\pi_{\zeta_{k,i} \rightarrow s_{k,i}} \prod_{j \in \mathcal{J}} \lambda_{k,i}^j}{\pi_{\zeta_{k,i} \rightarrow s_{k,i}} \prod_{j \in \mathcal{J}} \lambda_{k,i}^j + (1 - \pi_{\zeta_{k,i} \rightarrow s_{k,i}}) \prod_{j \in \mathcal{J}} (1 - \lambda_{k,i}^j)}. \quad (29b)$$

The message from ψ_k to α_k is given by

$$\varpi_{\psi_k \rightarrow \alpha_k} \propto \int_{\ell_k} \psi(\ell_k, \alpha_k) \varpi_{\chi_k \rightarrow \ell_k} = \pi_{\psi_k \rightarrow \alpha_k} \delta(\alpha_k - 1) + (1 - \pi_{\psi_k \rightarrow \alpha_k}) \delta(\alpha_k), \quad (30a)$$

with $\varpi_{\ell_k \rightarrow \psi_k} = \varpi_{\chi_k \rightarrow \ell_k}$, where

$$\pi_{\psi_k \rightarrow \alpha_k} = \frac{\pi_{\psi_k \rightarrow \alpha_k, 1}}{\pi_{\psi_k \rightarrow \alpha_k, 1} + \pi_{\psi_k \rightarrow \alpha_k, 0}}, \quad (30b)$$

$$\pi_{\psi_k \rightarrow \alpha_k, 1} = \frac{e^{-(m_{\chi_k \rightarrow \ell_k} - m_\psi)^2 / (2\sigma_{\chi_k \rightarrow \ell_k}^2 + 2\sigma_\psi^2)}}{\sqrt{2\pi(\sigma_{\chi_k \rightarrow \ell_k}^2 + \sigma_\psi^2)}}, \quad (30c)$$

$$\pi_{\psi_k \rightarrow \alpha_k, 0} = \frac{e^{-(-1 - m_{\chi_k \rightarrow \ell_k})^2 / 2\sigma_{\chi_k \rightarrow \ell_k}^2}}{\sqrt{2\pi\sigma_{\chi_k \rightarrow \ell_k}^2}}. \quad (30d)$$

The message from ψ_k to ℓ_k is constant and given by

$$\varpi_{\psi_k \rightarrow \ell_k} = \int_{\alpha_k} p(\alpha_k) \psi(\ell_k, \alpha_k) = \rho \mathcal{N}(\ell_k; m_\psi, \sigma_\psi^2) + (1 - \rho) \delta(\ell_k + 1). \quad (31)$$

Then we calculate the message from χ_k to $s_{k,i}$ with a similar form of (26b). To obtain $\pi_{\chi_k \rightarrow s_{k,i}}$, we first calculate $\lambda_{\chi_k \rightarrow s_{k,i}}$ based on the sum-product rule:

$$\begin{aligned} \lambda_{\chi_k \rightarrow s_{k,i}} &= \int_{\mathbf{s}_k \setminus s_{k,i}, \ell_k} \prod_{i' \neq i} \left(\varpi_{\zeta_{k,i'} \rightarrow s_{k,i'}} \prod_{j \in \mathcal{J}} \varpi_{k,i'}^j \right) \varpi_{\psi_k \rightarrow \ell_k} \delta \left(\ell_k - \sum_i s_{k,i} \right) \\ &= \int_{\ell_k} \varpi_{\psi_k \rightarrow \ell_k} \int_{\mathbf{s}_k \setminus s_{k,i}} \prod_{i' \neq i} \left(\varpi_{\zeta_{k,i'} \rightarrow s_{k,i'}} \prod_{j \in \mathcal{J}} \varpi_{k,i'}^j \right) \delta \left(\ell_k - s_{k,i} - \sum_{i' \neq i} s_{k,i'} \right), \end{aligned} \quad (32)$$

where $\mathbf{s}_k \setminus s_{k,i}$ denotes all the entries of \mathbf{s}_k except $s_{k,i}$. The inner integral is approximated by

$$\mathcal{N}(\ell_k - s_{k,i}; m_{\chi_k \rightarrow s_{k,i}}, \sigma_{\chi_k \rightarrow s_{k,i}}^2), \quad (33a)$$

where $m_{\chi_k \rightarrow s_{k,i}}$ and $\sigma_{\chi_k \rightarrow s_{k,i}}^2$ are respectively given by

$$m_{\chi_k \rightarrow s_{k,i}} = \sum_{i' \neq i} (2\pi_{s_{k,i'} \rightarrow \chi_k} - 1), \quad (33b)$$

$$\sigma_{\chi_k \rightarrow s_{k,i}}^2 = 4 \sum_{i' \neq i} \pi_{s_{k,i'} \rightarrow \chi_k} (1 - \pi_{s_{k,i'} \rightarrow \chi_k}). \quad (33c)$$

As such, $\lambda_{\chi_k \rightarrow s_{k,i}}$ can be given by

$$\lambda_{\chi_k \rightarrow s_{k,i}} = (1 - \rho) \mathcal{N}(s_{k,i}; LJ + m_{\chi_k \rightarrow s_{k,i}}, \sigma_{\chi_k \rightarrow s_{k,i}}^2) + \rho \mathcal{N}(s_{k,i}; m_{\chi_k \rightarrow s_{k,i}} m_{\psi}, \sigma_{\chi_k \rightarrow s_{k,i}}^2 + \sigma_{\psi}^2). \quad (34)$$

Then, $\pi_{\chi_k \rightarrow s_{k,i}}$ is given by

$$\pi_{\chi_k \rightarrow s_{k,i}} = \frac{\lambda_{\chi_k \rightarrow s_{k,i}}(s_{k,i} = 1)}{\lambda_{\chi_k \rightarrow s_{k,i}}(s_{k,i} = 1) + \lambda_{\chi_k \rightarrow s_{k,i}}(s_{k,i} = -1)}. \quad (35)$$

The output message of $s_{k,i}$ can be calculated as

$$\varpi_{s_{k,i} \rightarrow \zeta_{k,i}} = \pi_{s_{k,i} \rightarrow \zeta_{k,i}} \delta(s_{k,i} - 1) + (1 - \pi_{s_{k,i} \rightarrow \zeta_{k,i}}) \delta(s_{k,i} + 1), \quad (36a)$$

where

$$\pi_{s_{k,i} \rightarrow \zeta_{k,i}} = \frac{\pi_{\chi_k \rightarrow s_{k,i}} \prod_{j \in \mathcal{J}} \lambda_{k,i}^j}{\pi_{\chi_k \rightarrow s_{k,i}} \prod_{j \in \mathcal{J}} \lambda_{k,i}^j + (1 - \pi_{\chi_k \rightarrow s_{k,i}}) \prod_{j \in \mathcal{J}} (1 - \lambda_{k,i}^j)}. \quad (36b)$$

With $\varpi_{s_{k,i} \rightarrow \zeta_{k,i}}$, the message from $\zeta_{k,i}$ to $v_{k,i}$ is a Bernoulli-Gamma distribution given by

$$\varpi_{\zeta_{k,i} \rightarrow v_{k,i}} \propto \int_{s_{k,i}} p(v_{k,i} | s_{k,i}) \varpi_{s_{k,i} \rightarrow \zeta_{k,i}} = \pi_{s_{k,i} \rightarrow \zeta_{k,i}} \text{Gamma}(v_{k,i}; \gamma_{k,1}, \gamma_{k,2}) + (1 - \pi_{s_{k,i} \rightarrow \zeta_{k,i}}) \delta(v_{k,i}). \quad (37)$$

With $\varpi_{v_{k,i} \rightarrow \eta_{k,i}} = \varpi_{\zeta_{k,i} \rightarrow v_{k,i}}$, the message from $\eta_{k,i}$ to $h_{k,i}$ is given by

$$\varpi_{\eta_{k,i} \rightarrow h_{k,i}} \propto \int_{v_{k,i}} p(h_{k,i} | v_{k,i}) \varpi_{v_{k,i} \rightarrow \eta_{k,i}}. \quad (38)$$

The message from $h_{k,i}$ to ι is $\varpi_{h_{k,i} \rightarrow \iota} = \varpi_{\eta_{k,i} \rightarrow h_{k,i}}$. The message from ι to $h_{k,i}$ is

$$\begin{aligned} \varpi_{\iota \rightarrow h_{k,i}} &\propto \int_{\mathbf{h} \setminus h_{k,i}} p(\mathbf{y} | \mathbf{h}) \prod_{i' \neq i} \varpi_{\eta_{k,i'} \rightarrow \iota} \prod_{k' \neq k} \prod_{i''} \varpi_{\eta_{k',i''} \rightarrow \iota} \\ &= \int_{\mathbf{h} \setminus h_{k,i}} p(\mathbf{y} | \mathbf{h}) \prod_{i' \neq i} \int_{v_{k,i'}} p(x_{k,i'} | v_{k,i'}) \varpi_{v_{k,i'} \rightarrow \eta_{k,i'}} \prod_{k' \neq k} \prod_{i''} \int_{v_{k',i''}} p(x_{k',i''} | v_{k',i''}) \varpi_{v_{k',i''} \rightarrow \eta_{k',i''}}, \end{aligned} \quad (39)$$

where $\mathbf{h} \setminus h_{k,i}$ denotes all the entries of \mathbf{h} except $h_{k,i}$. Clearly, $\varpi_{h_{k,i} \rightarrow \eta_{k,i}} = \varpi_{\iota \rightarrow h_{k,i}}$. Then, the messages $\varpi_{\eta_{k,i} \rightarrow v_{k,i}}$ and $\varpi_{v_{k,i} \rightarrow \zeta_{k,i}}$ can be computed as

$$\varpi_{v_{k,i} \rightarrow \zeta_{k,i}} = \varpi_{\eta_{k,i} \rightarrow v_{k,i}} \propto \int_{h_{k,i}} p(h_{k,i} | v_{k,i}) \varpi_{h_{k,i} \rightarrow \eta_{k,i}}. \quad (40)$$

Note that the integrals involved in (39) and (40) are difficult to evaluate. From [8], we can replace the output of the linear module for node $v_{k,i}$ by the mean $\mu_{\eta_{k,i} \rightarrow v_{k,i}} = \mathbb{E}_{\varpi_{\eta_{k,i} \rightarrow v_{k,i}}} [v_{k,i}]$.

Then $\varpi_{\eta_{k,i} \rightarrow v_{k,i}}$ is approximated by

$$\mu_{\eta_{k,i} \rightarrow v_{k,i}} = \arg \max_{v_{k,i}} p(\mathbf{y} | \mathbf{v}) \Big|_{v_{k,i'} = \mu_{v_{k,i'} \rightarrow \eta_{k,i'}}, \forall i' \neq i}, \quad (41)$$

where $\mu_{v_{k,i} \rightarrow \eta_{k,i}}$ is the incoming mean of $v_{k,i}$ for the linear module, i.e., $\mu_{v_{k,i} \rightarrow \eta_{k,i}} = \mathbb{E}_{\varpi_{v_{k,i} \rightarrow \eta_{k,i}}} [v_{k,i}]$. Note that $p(\mathbf{h}|\mathbf{y}, \mathbf{v}) \propto p(\mathbf{y}|\mathbf{h})p(\mathbf{h}|\mathbf{v})$ is a complex Gaussian distribution with the mean \mathbf{m} and the covariance Φ given by

$$\mathbf{m} = \mathbf{D}\mathbf{A}^H(\sigma^{-2}\mathbf{I} + \mathbf{A}\mathbf{D}\mathbf{A}^H)^{-1}\mathbf{y}, \quad (42)$$

$$\Phi = \mathbf{D} - \mathbf{D}\mathbf{A}^H(\sigma^{-2}\mathbf{I} + \mathbf{A}\mathbf{D}\mathbf{A}^H)^{-1}\mathbf{A}\mathbf{D}, \quad (43)$$

where \mathbf{D} is a diagonal matrix with the $((k-1)LJ+i)$ -th diagonal element equals to $\mu_{v_{k,i} \rightarrow \eta_{k,i}}$. Hence, by using the ELBO-based method in [8], the solution of (41) can be obtained by

$$\mu_{\eta_{k,i} \rightarrow v_{k,i}} = |m_{(k-1)LJ+i}|^2 + \phi_{(k-1)LJ+i}, \quad (44)$$

where $m_{(k-1)LJ+i}$ and $\phi_{(k-1)LJ+i}$ are the $\{(k-1)LJ+i\}$ -th entry of \mathbf{m} and the $\{(k-1)LJ+i\}$ -th diagonal element of Φ , respectively. Then $\pi_{\zeta_{k,i} \rightarrow s_{k,i}}$ is approximated as

$$\pi_{\zeta_{k,i} \rightarrow s_{k,i}} = \min\left(\frac{\mu_{\eta_{k,i} \rightarrow v_{k,i}}}{\gamma_{k,1}/\gamma_{k,2}}, 1\right), \quad (45)$$

Similarly, $\varpi_{v_{k,i} \rightarrow \eta_{k,i}}$ can be approximated as

$$\mu_{v_{k,i} \rightarrow \eta_{k,i}} = \mathbb{E}_{\varpi_{v_{k,i} \rightarrow \eta_{k,i}}} [v_{k,i}] = \frac{\gamma_{k,1}}{\gamma_{k,2}} \pi_{s_{k,i} \rightarrow \zeta_{k,i}}. \quad (46)$$

Then, we approximate the mean of the Gamma distribution $\gamma_{k,1}/\gamma_{k,2}$ by κ_k , where κ_k is the mean of the largest $\lfloor 3LJ\rho_s \rfloor$ elements in $\{\mu_{\eta_{k,i} \rightarrow v_{k,i}}\}_{i=1}^{LJ}$. For inactive devices, this approximation is not accurate because $\{\mu_{\eta_{k,i} \rightarrow v_{k,i}}\}_{i=1}^{LJ}$ has no information about the Gamma distribution. To address this problem, we use the detected active devices' information to help inactive devices. Let $\kappa'_1 \geq \dots \geq \kappa'_K$ be the reordered sequence of $\kappa_1, \dots, \kappa_K$, and $K^+ = \sum_k \hat{\alpha}_k$ the number of detected active devices, where $\hat{\alpha}_k$ is given by (47). We suppose that the devices corresponding to the largest $\theta_1 K^+$ κ'_k s are active, and their κ_k s are calculated by $\lfloor 3LJ\rho_s \rfloor$, where $0 < \theta_1 < 1$. The left $K - \theta_1 K^+$ devices' κ_k is approximated by $1/(\theta_2 K^+) \sum_{k=1}^{\theta_2 K^+} \kappa'_k$, where $\theta_2 \geq 1$. The detailed derivation of the approximations in (41)-(46) can be found in [8].

The above messages are updated iteratively until the algorithm converges. Then, we use the estimate $\hat{\mathbf{h}} = \mathbf{m}$ to recover the channel $\hat{\mathbf{G}}_u$ based on (16a), and estimate the device activity as

$$\hat{\alpha}_k = \begin{cases} 1, & \text{if } \rho\pi_{\psi_k \rightarrow \alpha_k} > (1-\rho)(1-\pi_{\psi_k \rightarrow \alpha_k}), \\ 0, & \text{if } \rho\pi_{\psi_k \rightarrow \alpha_k} \leq (1-\rho)(1-\pi_{\psi_k \rightarrow \alpha_k}), \end{cases} \quad \forall k. \quad (47)$$

C. Overall Algorithm and Complexity

The overall MVSP algorithm is summarized in Algorithm 1. We now analyse the computational complexity of the MVSP algorithm. The complexity in step 5 is $\mathcal{O}(R^3 + R^2Q)$. The complexities in step 8, step 10 and step 11 are all $\mathcal{O}(Q)$. The complexity in step 13 is $\mathcal{O}(Q + K)$. Thus, the computational complexity of the MVSP algorithm is dominated by step 6, and is given by $\mathcal{O}(T_{\text{out}}(T_{\text{in1}}(R^3 + R^2Q + Q) + K))$.

Algorithm 1: MVSP algorithm

Input: \mathbf{y} , \mathbf{A} , T_{out} , T_{in1} , T_{in2}

```

1 for  $t_{\text{out}} = 1$  to  $T_{\text{out}}$  do
2    $\hat{\boldsymbol{\mu}} = [\mu_{v_{1,1} \rightarrow \eta_{1,1}}, \dots, \mu_{v_{K,LK} \rightarrow \eta_{K,LJ}}]^T$ ;
3   for  $t_{\text{in1}} = 1$  to  $T_{\text{in1}}$  do
4      $\mathbf{D} = \text{diag}(\hat{\boldsymbol{\mu}})$ ;
5     Compute  $\mathbf{m}$  and  $\Phi$  by using (42) and (43);
6     Update  $\hat{\boldsymbol{\mu}} = [\hat{\mu}_{\eta_{1,1} \rightarrow v_{1,1}}, \dots, \hat{\mu}_{\eta_{K,LJ} \rightarrow v_{K,LJ}}]^T$  with (44);
7   end
8   Compute  $\{\pi_{\zeta_{k,i} \rightarrow s_{k,i}}\}$  based on (45) and  $[\mu_{\eta_{1,1} \rightarrow v_{1,1}}, \dots, \mu_{\eta_{K,LJ} \rightarrow v_{K,LJ}}]^T = \hat{\boldsymbol{\mu}}$ ;
9   for  $t_{\text{in2}} = 1$  to  $T_{\text{in2}}$  do
10    Compute  $\{\varpi_{k,i}^j\}$  based on (26a);
11    Compute  $\{\pi_{\chi_k \rightarrow s_{k,i}}\}$  based on (33)-(35);
12  end
13  Compute  $\{\pi_{\chi_k \rightarrow \alpha_k}\}$ ,  $\{\hat{\alpha}_k\}$ , and  $\{\mu_{v_{k,i} \rightarrow \eta_{k,i}}\}$  by (30b), (47) and (46), respectively;
14 end

```

Output: $\hat{\mathbf{h}} = \mathbf{m}$, $\hat{\alpha}_k, \forall k$.

IV. EM-MVSP ALGORITHM

A. Model Mismatch Problem

It is worth noting that the true delay and Doppler frequency shift of each path may not fall onto the given grid $\boldsymbol{\tau}_k$ and $\boldsymbol{\nu}_k$, which results in the model mismatch problem. To tackle this, we treat $\boldsymbol{\tau}_k$ and $\boldsymbol{\nu}_k$ involved in \mathbf{A} as unknown parameters and consider a parametric dictionary learning method to improve the performance of the MVSP. To this end, we denote \mathbf{A} as $\mathbf{A}(\boldsymbol{\omega})$ where $\boldsymbol{\omega} = \{\boldsymbol{\tau}_1, \dots, \boldsymbol{\tau}_K, \boldsymbol{\nu}_1, \dots, \boldsymbol{\nu}_K\}$. We learn the parameter set $\boldsymbol{\omega}$ through the EM method.

B. EM Framework

Each iteration of the EM method consists of two steps:

- E-step: To calculate the posterior distribution of hidden variables based on the estimates obtained in the previous iteration, and then formulate a function \mathcal{Q} which is the posterior mean of the log-likelihood function with respect to the hidden variables;
- M-step: To maximize \mathcal{Q} with respect to the hidden variables to update parameters.

E-Step and M-step iterate until converge. In our problem, the observed variables are the received signal \mathbf{y} in (15), the hidden variables are the channel representation vector \mathbf{h} , and the parameters to be estimated are $\boldsymbol{\omega}$. Note that the MVSP algorithm can provide approximate posterior distributions of \mathbf{h} in the iteration. Therefore, in this problem, the key to update $\boldsymbol{\omega}$ is the M-step, i.e., to maximize the posterior mean of the log-likelihood function \mathcal{Q} . Denote by $\boldsymbol{\omega}^{(i)}$ the parameter update obtained in the i -th iteration. Then the \mathcal{Q} function is formulated as

$$\begin{aligned}\mathcal{Q}(\boldsymbol{\omega}, \boldsymbol{\omega}^{(i)}) &= \int_{\mathbf{h}} \ln p(\mathbf{y}, \mathbf{h} | \boldsymbol{\omega}) p(\mathbf{h} | \mathbf{y}, \boldsymbol{\omega}^{(i)}) \\ &= \int_{\mathbf{h}} \ln p(\mathbf{y} | \mathbf{h}, \boldsymbol{\omega}) p(\mathbf{h} | \mathbf{y}, \boldsymbol{\omega}^{(i)}) \int_{\mathbf{h}} \ln p(\mathbf{h}) p(\mathbf{h} | \mathbf{y}, \boldsymbol{\omega}^{(i)}) .\end{aligned}\quad (48)$$

Note that the second term in (48) is irrelevant to $\boldsymbol{\omega}$. Therefore, M-step is equivalent to minimizing

$$\mathcal{F}(\boldsymbol{\omega}, \boldsymbol{\omega}^{(i)}) = - \int_{\mathbf{h}} \ln p(\mathbf{y} | \mathbf{h}, \boldsymbol{\omega}) p(\mathbf{h} | \mathbf{y}, \boldsymbol{\omega}^{(i)}) .\quad (49)$$

From the additive CSCG noise model in (15), we have

$$p(\mathbf{y} | \mathbf{h}, \boldsymbol{\omega}) = \mathcal{CN}(\mathbf{y} - \mathbf{A}(\boldsymbol{\omega}) \mathbf{h}; \mathbf{0}, \sigma^2 \mathbf{I}) .\quad (50)$$

In each outer iteration of the MVSP algorithm, the posterior distribution of the channel representation \mathbf{h} given by the linear module is approximated by

$$p(\mathbf{h} | \mathbf{y}, \boldsymbol{\omega}^{(i)}) = \mathcal{CN}(\mathbf{h} - \mathbf{m}(\boldsymbol{\omega}^{(i)}); \mathbf{0}, \boldsymbol{\Phi}(\boldsymbol{\omega}^{(i)})) ,\quad (51)$$

where $\mathbf{m}(\boldsymbol{\omega}^{(i)})$ and $\boldsymbol{\Phi}(\boldsymbol{\omega}^{(i)})$ are the posterior mean and the covariance matrix of \mathbf{h} calculated based on \mathbf{y} and $\mathbf{A}(\boldsymbol{\omega}^{(i)})$. Plugging (50) and (51) into (49), we have

$$\begin{aligned}\mathcal{F}(\boldsymbol{\omega}, \boldsymbol{\omega}^{(i)}) &= \frac{1}{\sigma^2} \int_{\mathbf{h}} \left(\mathbf{y}^H \mathbf{y} - \mathbf{y}^H \mathbf{A}(\boldsymbol{\omega}) \mathbf{h} - \mathbf{y}^H \mathbf{A}^H(\boldsymbol{\omega}) \mathbf{y} \right. \\ &\quad \left. + \mathbf{h}^H \mathbf{A}^H(\boldsymbol{\omega}) \mathbf{A}(\boldsymbol{\omega}) \mathbf{h} \right) p(\mathbf{h} | \mathbf{y}, \boldsymbol{\omega}^{(i)}) + \ln(\pi \sigma^2) .\end{aligned}\quad (52)$$

Remove the irrelevant terms in (52) and define a new objective function

$$\begin{aligned}
\mathcal{G}(\boldsymbol{\omega}, \boldsymbol{\omega}^{(i)}) &= \int_{\mathbf{h}} \left(-\mathbf{y}^H \mathbf{A}(\boldsymbol{\omega}) \mathbf{h} - \mathbf{h}^H \mathbf{A}^H(\boldsymbol{\omega}) \mathbf{y} + \mathbf{h}^H \mathbf{A}^H(\boldsymbol{\omega}) \mathbf{A}(\boldsymbol{\omega}) \mathbf{h} \right) p(\mathbf{h}|\mathbf{y}, \boldsymbol{\omega}^{(i)}) \\
&= -2\mathcal{R}(\mathbf{y}^H \mathbf{A}(\boldsymbol{\omega}) \mathbf{m}(\boldsymbol{\omega}^{(i)})) + \text{Tr} \left(\mathbf{A}^H(\boldsymbol{\omega}) \mathbf{A}(\boldsymbol{\omega}) \int_{\mathbf{h}} \mathbf{h} \mathbf{h}^H p(\mathbf{h}|\mathbf{y}, \boldsymbol{\omega}^{(i)}) \right) \\
&= -2\mathcal{R}(\mathbf{y}^H \mathbf{A}(\boldsymbol{\omega}) \mathbf{m}(\boldsymbol{\omega}^{(i)})) + \text{Tr} \left(\mathbf{A}^H(\boldsymbol{\omega}) \mathbf{A}(\boldsymbol{\omega}) \boldsymbol{\Omega}^{(i)} \right), \tag{53}
\end{aligned}$$

where $\boldsymbol{\Omega}^{(i)} = \boldsymbol{\Phi}(\boldsymbol{\omega}^{(i)}) + \mathbf{m}(\boldsymbol{\omega}^{(i)}) \mathbf{m}^H(\boldsymbol{\omega}^{(i)})$.

In summary, in each update of $\boldsymbol{\omega}$ through EM, our method is to calculate the posterior distribution of \mathbf{h} and construct the objective function $\mathcal{G}(\boldsymbol{\omega}, \boldsymbol{\omega}^{(i)})$ based on \mathbf{y} and $\boldsymbol{\Omega}^{(i)}$. It is not easy to obtain an analytical solution to this problem with respect to both $\boldsymbol{\tau}_k$ and $\boldsymbol{\nu}_k$. Therefore, we use the gradient descent method to minimize $\mathcal{G}(\boldsymbol{\omega}, \boldsymbol{\omega}^{(i)})$ and then update $\boldsymbol{\omega}$ in each iteration.

Algorithm 2: EM-MVSP algorithm

Input: \mathbf{y} , $\{\mathbf{x}_u\}$, T_{out} , T_{in} , i_{max} .

- 1 Initialization: $i = 0$, $\boldsymbol{\omega}^{(0)} = \{\boldsymbol{\tau}_1^{(0)}, \dots, \boldsymbol{\tau}_K^{(0)}, \boldsymbol{\nu}_1^{(0)}, \dots, \boldsymbol{\nu}_K^{(0)}\}$;
 - 2 **while** the stopping criterion is not met **do**
 - 3 Generate $\mathbf{A}(\boldsymbol{\omega}^{(i)})$ based on $\boldsymbol{\omega}^{(i)}$ and $\{\mathbf{x}_u\}$;
 - 4 With \mathbf{y} and $\mathbf{A}(\boldsymbol{\omega}^{(i)})$, calculate $\mathbf{m}(\boldsymbol{\omega}^{(i)})$, $\boldsymbol{\Phi}(\boldsymbol{\omega}^{(i)})$ and $\hat{\alpha}_k(\boldsymbol{\omega}^{(i)})$ by Algorithm 1;
 - 5 Minimize (53) with respect to $\boldsymbol{\tau}_k$, and obtain the updated $\boldsymbol{\tau}_k^{(i+1)}$, $\forall k$;
 - 6 Minimize (53) with respect to $\boldsymbol{\nu}_k$, and obtain the updated $\boldsymbol{\nu}_k^{(i+1)}$, $\forall k$;
 - 7 $\boldsymbol{\omega}^{(i+1)} = \{\boldsymbol{\tau}_1^{(i+1)}, \dots, \boldsymbol{\tau}_K^{(i+1)}, \boldsymbol{\nu}_1^{(i+1)}, \dots, \boldsymbol{\nu}_K^{(i+1)}\}$, $i = i + 1$;
 - 8 **end**
- Output:** $\hat{\mathbf{h}} = \mathbf{m}(\boldsymbol{\omega}^{(i)})$, $\hat{\alpha}_k = \hat{\alpha}_k(\boldsymbol{\omega}^{(i)})$.
-

C. Overall Algorithm and Complexity

Algorithm 2 summarizes the EM-MVSP algorithm. The stopping criterion of the iteration is generally set to “ $\|\boldsymbol{\omega}^{(i+1)} - \boldsymbol{\omega}^{(i)}\|^2$ is less than a small positive threshold or $i \geq i_{\text{max}}$ ”, where i_{max} is the maximal number of iterations of the EM. We now analyse the computational complexity of the EM-MVSP algorithm. The complexity in step 3 is $\mathcal{O}(RQ(M + LJ))$. The complexities in step 5 and step 6 are both $\mathcal{O}(Q^3 + Q^2R)$. As mentioned in Section IV-C, the complexity in step 4 is $\mathcal{O}(T_{\text{out}}T_{\text{in}}(R^3 + R^2Q))$. Thus, the computational complexity of the EM-MVSP algorithm is given by $\mathcal{O}(i_{\text{max}}(Q^3 + Q^2R + T_{\text{out}}(T_{\text{in}}(R^3 + R^2Q + Q) + K)))$.

V. SIMULATION RESULTS

In this section, we carry out simulations to demonstrate the effectiveness of the proposed algorithms. The CE and DAD performance are respectively measured in terms of NMSE and detection error probability $P_e = \mathbb{E}[1/K \sum_k (p(\hat{\alpha}_k = 0|\alpha_k = 1) + p(\hat{\alpha}_k = 1|\alpha_k = 0))]$ over 100 independent trials. The signal-noise-ratio (SNR) is defined as $\sum_u \|\mathbf{G}_u \mathbf{x}_u\|^2 / (R\sigma^2)$. The baseline methods used for comparison includes OMP [28], GAMP [29], structured TCS (STCS) [30], SBL [6], and pattern-coupled SBL (PCSBL) [31]. The iteration number of EM in EM-MVSP is 4. $\{x_{k,m,u}\}$ are generated from the standard complex Gaussian distribution. The parameters in the simulation are listed as follows. The satellite operates at a speed of 7 km/s in an orbit of 600 km, and the coverage of the beam is a circle with a diameter of 50 km. As shown in Fig. 7, device A and device B are at the border of the beam coverage, and the elevation angle between the satellite and device A is α_e . The velocity of devices follows the uniform distribution with [0, 120] km/h, the delay spreading is 0.5 μ s, the length of CP is $T_{cp} = 2 \mu$ s. We adopt the TDL-A channel model in [34]. The large scale fading is compensated since it changes slightly over the devices in a beam. The total number of OFDM symbols in a transmission frame is $UN = 12$, and the subcarrier spacing is $\Delta f = 15$ kHz.

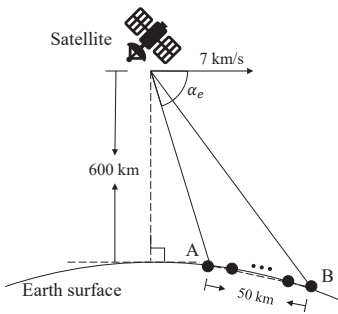


Fig. 7. Illustration of the simulated satellite-IoT system.

We first consider the scenario when there is no mismatch between the real channel and the grid-based model, that is, the delay and the Doppler frequency shift of each channel path fall onto the delay-Doppler grid. In Fig. 8(a) we show the CE NMSE versus the SNR. The proposed MVSP outperforms other baseline methods as SNR increases. In particular, due to the special structure of the measurement matrix discussed in Section II-E, we notice that GAMP and STCS behave poorly in this task, with a NMSE about 0 dB. PCSBL outperforms SBL but still has a large performance gap with the proposed MVSP algorithm. In the SNR range of [16, 24] dB,

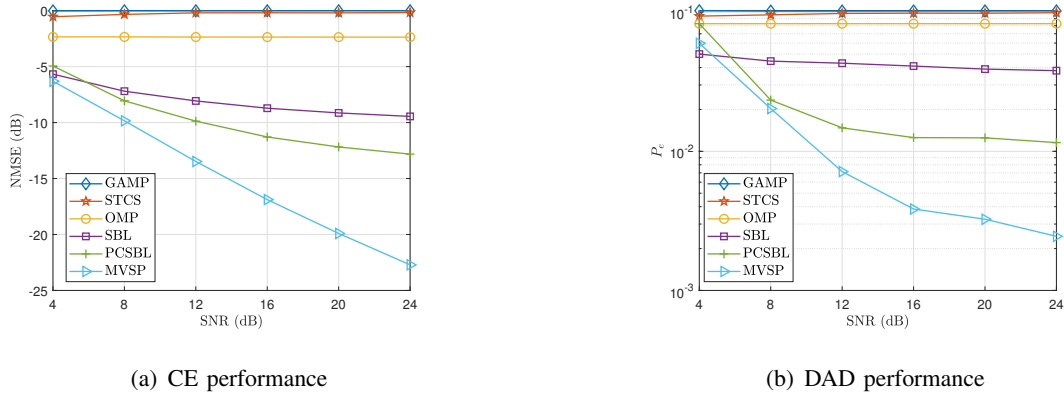


Fig. 8. CE and DAD performances under various SNR and on-grid settings. Related parameters are $K = 200$, $\rho = 0.1$, $N = 4$, $L = 4$, $J = 24$, $M = 32$ and $\alpha_e = 50^\circ$.

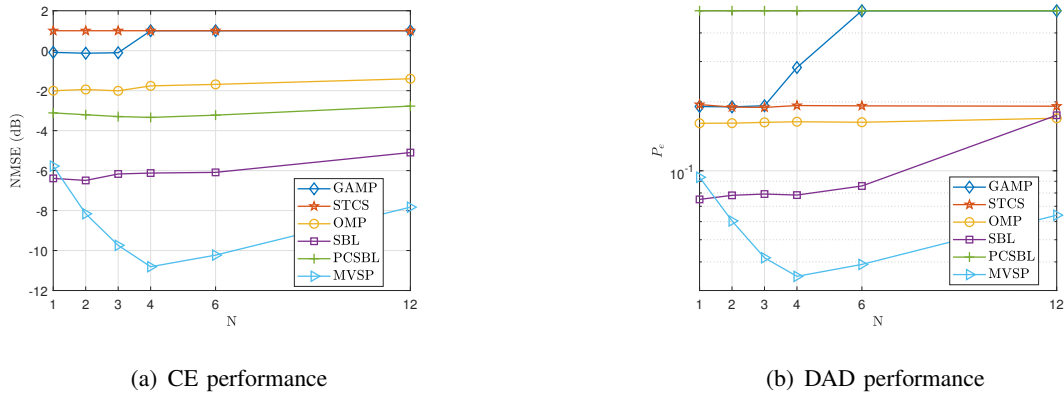


Fig. 9. CE and DAD performances under various number of cascaded OFDM symbols N and off-grid settings. Related parameters are $K = 100$, $\rho = 0.2$, $L = 6$, $J = 20$, SNR=20 dB, $M = 16$ and $\alpha_e = 70^\circ$.

the MVSP algorithm is at least 5 dB better than other baseline methods in NMSE. Fig. 8(b) shows the detection error probability versus the SNR. We see that as the SNR increases, the P_e of GAMP, STCS, OMP and SBL can hardly be improved. MVSP obviously outperform the baseline methods, especially when the SNR is over 16 dB.

We further consider the mismatch between the real channel and the grid-based model, namely, the off-grid scenario. Fig. 9(a) shows the NMSE against the number of repeated OFDM symbols N in a super-symbol. As N increases, it is interesting that different methods have different trends since more repeated OFDM symbols can improve the frequency resolution, but also results in the correlation of measurement matrix. The NMSEs of GAMP and OMP increase because they are sensitive to measurement matrix, and repeated OFMD symbols results in performance

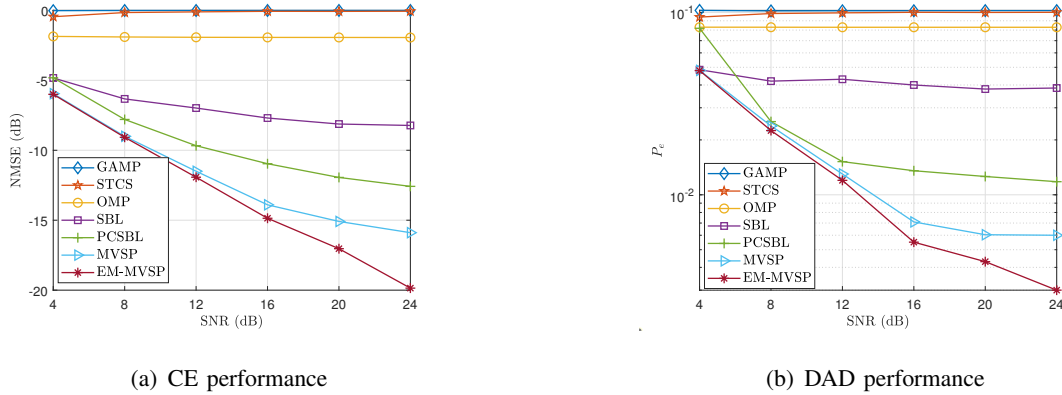


Fig. 10. CE and DAD performances under various SNR and off-grid settings, and $\alpha_e = 50^\circ$. Related parameters are $K = 200$, $\rho = 0.1$, $N = 4$, $L = 4$, $J = 24$ and $M = 32$.

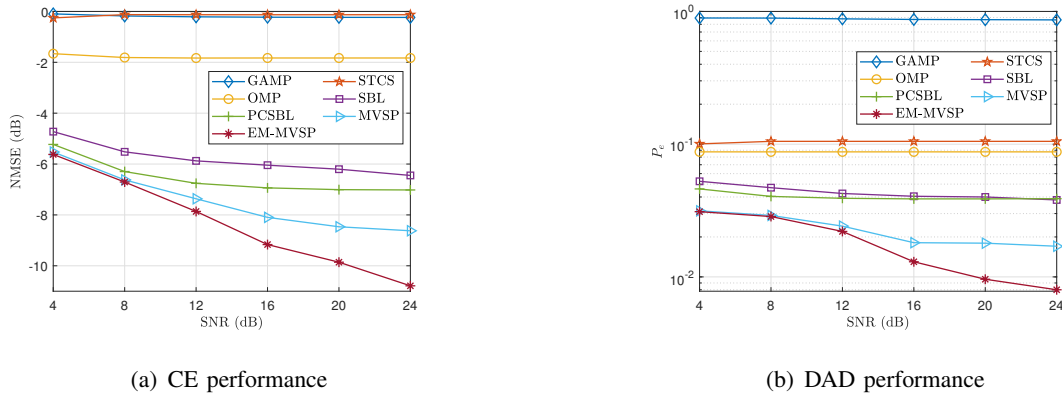


Fig. 11. CE and DAD performances under various SNR and off-grid settings, and $\alpha_e = 90^\circ$. Related parameters are $K = 200$, $\rho = 0.1$, $N = 4$, $L = 4$, $J = 24$ and $M = 32$.

degradation. As for PCSBL and SBL, their NMSEs first slightly decrease and then increase. Then, MVSP are more robust to the measurement matrix, with significant performance gain as N increases. We see that for MVSP more than 4 dB gain can be obtained from repeated OFDM symbols. When $N > 4$, almost all the algorithms have a performance degradation due to the measurement matrix correlation. In Fig. 10(a), we show detection error probability against N . The trade off between frequency resolution improvement and measurement matrix correlation is also obvious, which demonstrates the effectiveness of cascaded OFDM symbols.

Then we show the NMSE performance against the SNR with $\alpha_e = 50^\circ$ in Fig. 10(a). As the SNR increases, MVSP and EM-MVSP are at least 4 and 6 dB better than other baseline methods in NMSE, respectively. The proposed algorithms also behave well in DAD as shown in Fig. 10(b).

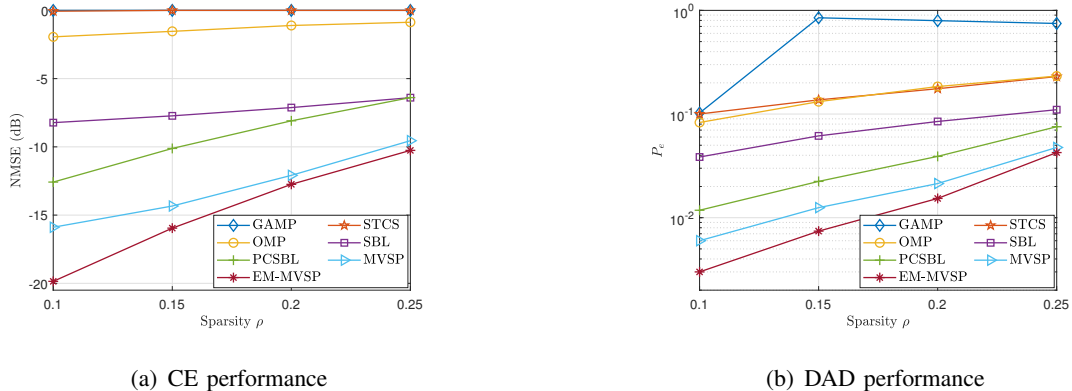


Fig. 12. CE and DAD performances under various sparsity ρ and off-grid settings. Related parameters are $K = 200$, $N = 4$, $L = 4$, $J = 20$, $\text{SNR} = 24$ dB, $M = 32$ and $\alpha_e = 50^\circ$.

We notice that PCSBL, MVSP and EM-MVSP have a significant performance gap compared with other methods in the considered SNR range, and their performance is similar at a lower SNR. This is because these three methods all consider the channel block-sparsity structure, but one-dimension block-sparsity in PCSBL and two-dimension block-sparsity in MVSP and EM-MVSP. In Fig. 11, we further consider the scenario with elevation angle $\alpha_e = 90^\circ$, where the Doppler effect is more severe. We see that MVSP and EM-MVSP still outperform the baselines. Compared with PCSBL, EM-MVSP have a performance gain of more than 3 dB in NMSE and one order of magnitude in P_e . Thus, the proposed MVSP and EM-MVSP algorithms show performance advantages under different Doppler effects.

Fig. 12 shows the CE and DAD performances of all the algorithms under varying sparsity ρ . The proposed MVSP and EM-MVSP have a considerable performance gap within the considered sparsity range. Even at $\rho = 0.2$, i.e., about 40 active devices access to the satellite, P_e of EM-MVSP can reach 10^{-2} , which demonstrates the advantage of the proposed algorithms for massive connectivity in satellite-IoT systems.

VI. CONCLUSION

In this paper, we studied the joint DAD and CE for GF-NORA in LEO satellite-IoT. We developed an OFDM-symbol repetition technique to better distinguish the Doppler shifts of the LEO satellite channel. We established a grid-based parametric system model, and showed that joint DAD and CE can be formulated as a CS problem. However, we pointed out that the measurement matrix of the problem exhibits special correlation structure, so that existing

Bayesian CS algorithms such as AMP and Turbo-CS do not behave well. To address this issue, we proposed the MVSP algorithm which is robust to the sensing matrix and can efficiently exploit the channel sparsity in the delay-Doppler-user domain. We then used the EM method to learn the grid parameters and further improve the performance of MVSP. Simulation results demonstrated that the proposed algorithms significantly outperform the counterparts methods.

REFERENCES

- [1] L. Atzori, A. Iera, and G. Morabito, "The internet of things: A survey," *Comput. Netw.*, vol. 54, no. 15, pp. 2787–2805, Oct. 2010.
- [2] J. Chen, K. Hu, Q. Wang, Y. Sun, Z. Shi, and S. He, "Narrowband internet of things: Implementations and applications," *IEEE Internet Things J.*, vol. 4, no. 6, pp. 2309–2314, Dec. 2017.
- [3] L. Liu, E. G. Larsson, W. Yu, P. Popovski, C. Stefanovic, and E. de Carvalho, "Sparse signal processing for grant-free massive connectivity: A future paradigm for random access protocols in the internet of things," *IEEE Signal Process. Mag.*, vol. 35, no. 5, pp. 88–99, Sept. 2018.
- [4] J. Ding, M. Nemat, C. Ranaweera, and J. Choi, "IoT connectivity technologies and applications: A survey," *IEEE Access*, vol. 8, pp. 67 646–67 673, 2020.
- [5] D. L. Donoho, A. Maleki, and A. Montanari, "Message-passing algorithms for compressed sensing," *Proc. Nat. Acad. Sci.*, vol. 106, no. 45, pp. 18 914–18 919, Nov. 2009.
- [6] M. E. Tipping, "Sparse Bayesian learning and the relevance vector machine," *J. Mach. Learn. Res.*, vol. 1, pp. 211–244, Sept. 2001.
- [7] J. Ma, X. Yuan, and L. Ping, "Turbo compressed sensing with partial DFT sensing matrix," *IEEE Signal Process. Lett.*, vol. 22, no. 2, pp. 158–161, Feb. 2015.
- [8] M. Zhang, X. Yuan, and Z.-Q. He, "Variance state propagation for structured sparse Bayesian learning," *IEEE Trans. Signal Process.*, vol. 68, pp. 2386–2400, Mar. 2020.
- [9] Z. Chen, F. Sohrabi, and W. Yu, "Sparse activity detection for massive connectivity," *IEEE Trans. Signal Process.*, vol. 66, no. 7, pp. 1890–1904, Apr. 2018.
- [10] T. Liu, S. Jin, C.-K. Wen, M. Matthaiou, and X. You, "Generalized channel estimation and user detection for massive connectivity with mixed-ADC massive MIMO," *IEEE Trans. Wireless Commun.*, vol. 18, no. 6, pp. 3236–3250, Jun. 2019.
- [11] M. Ke, Z. Gao, Y. Wu, X. Gao, and R. Schober, "Compressive sensing-based adaptive active user detection and channel estimation: Massive access meets massive MIMO," *IEEE Trans. Signal Process.*, vol. 68, pp. 764–779, Jan. 2020.
- [12] Z. Zhang, Y. Li, C. Huang, Q. Guo, C. Yuen, and Y. L. Guan, "DNN-aided block sparse Bayesian learning for user activity detection and channel estimation in grant-free non-orthogonal random access," *IEEE Trans. Veh. Technol.*, vol. 68, no. 12, pp. 12 000–12 012, Dec. 2019.
- [13] Q. Zou, H. Zhang, D. Cai, and H. Yang, "A low-complexity joint user activity, channel and data estimation for grant-free massive MIMO systems," *IEEE Signal Process. Lett.*, vol. 27, pp. 1290–1294, Jul. 2020.
- [14] T. Ding, X. Yuan, and S. C. Liew, "Sparsity learning-based multiuser detection in grant-free massive-device multiple access," *IEEE Trans. Wireless Commun.*, vol. 18, no. 7, pp. 3569–3582, Jul. 2019.
- [15] M. De Sanctis, E. Cianca, G. Araniti, I. Bisio, and R. Prasad, "Satellite communications supporting internet of remote things," *IEEE Internet Things J.*, vol. 3, no. 1, pp. 113–123, Feb. 2016.

- [16] M. Asad Ullah, K. Mikhaylov, and H. Alves, "Massive machine-type communication and satellite integration for remote areas," *IEEE Wireless Commun.*, vol. 28, no. 4, pp. 74–80, Aug. 2021.
- [17] M. Centenaro, C. E. Costa, F. Granelli, C. Sacchi, and L. Vangelista, "A survey on technologies, standards and open challenges in satellite IoT," *IEEE Commun. Surv. Tutorials.*, vol. 23, no. 3, pp. 1693–1720, May 2021.
- [18] X. Lin, B. Hofström, Y.-P. E. Wang, G. Masini, H.-L. Maattanen, H. Rydén, J. Sedin, M. Stattin, O. Liberg, S. Euler *et al.*, "5G new radio evolution meets satellite communications: Opportunities, challenges, and solutions," in *5G and Beyond*. Springer, 2021, pp. 517–531.
- [19] A. Gaber, M. A. ElBahaay, A. Maher Mohamed, M. M. Zaki, A. Samir Abdo, and N. AbdelBaki, "5G and satellite network convergence: Survey for opportunities, challenges and enabler technologies," in *2020 2nd Novel Intelligent and Leading Emerging Sciences Conference (NILES)*, Giza, Egypt, 2020, pp. 366–373.
- [20] O. Kodheli, A. Guidotti, and A. Vanelli-Coralli, "Integration of satellites in 5G through LEO constellations," in *Proc. IEEE Global Commun. Conf. (GLOBECOM)*, Singapore, Jan. 2017, pp. 1–6.
- [21] Z. Zhang, Y. Li, C. Huang, Q. Guo, L. Liu, C. Yuen, and Y. L. Guan, "User activity detection and channel estimation for grant-free random access in LEO satellite-enabled internet of things," *IEEE Internet Things J.*, vol. 7, no. 9, pp. 8811–8825, Sept. 2020.
- [22] L. Zhen, H. Qin, B. Song, R. Ding, X. Du, and M. Guizani, "Random access preamble design and detection for mobile satellite communication systems," *IEEE J. Sel. Areas Commun.*, vol. 36, no. 2, pp. 280–291, Feb. 2018.
- [23] L. Zhen, A. K. Bashir, K. Yu, Y. D. Al-Otaibi, C. H. Foh, and P. Xiao, "Energy-efficient random access for LEO satellite-assisted 6G internet of remote things," *IEEE Internet Things J.*, vol. 8, no. 7, pp. 5114–5128, Apr. 2021.
- [24] Y. Liu and Z. Tan, "Carrier frequency offset estimation for OFDM systems using repetitive patterns," *Radioengineering*, vol. 21, no. 3, pp. 823–830, 2012.
- [25] M. Morelli and U. Mengali, "Carrier-frequency estimation for transmissions over selective channels," *IEEE Trans. Commun.*, vol. 48, no. 9, pp. 1580–1589, Sept. 2000.
- [26] J.-W. Choi, J. Lee, Q. Zhao, and H.-L. Lou, "Joint ml estimation of frame timing and carrier frequency offset for OFDM systems employing time-domain repeated preamble," *IEEE Trans. Wireless Commun.*, vol. 9, no. 1, pp. 311–317, Jan. 2010.
- [27] H. Minn, V. Bhargava, and K. Letaief, "A robust timing and frequency synchronization for OFDM systems," *IEEE Trans. Wireless Commun.*, vol. 2, no. 4, pp. 822–839, July 2003.
- [28] J. A. Tropp and A. C. Gilbert, "Signal recovery from random measurements via orthogonal matching pursuit," *IEEE Trans. Inf. Theory.*, vol. 53, no. 12, pp. 4655–4666, Dec. 2007.
- [29] Z.-Q. He, X. Yuan, and L. Chen, "Super-resolution channel estimation for massive MIMO via clustered sparse Bayesian learning," *IEEE Trans. Veh. Technol.*, vol. 68, no. 6, pp. 6156–6160, Jun. 2019.
- [30] L. Chen, A. Liu, and X. Yuan, "Structured turbo compressed sensing for massive MIMO channel estimation using a Markov prior," *IEEE Trans. Veh. Technol.*, vol. 67, no. 5, pp. 4635–4639, May 2018.
- [31] J. Fang, Y. Shen, H. Li, and P. Wang, "Pattern-coupled sparse Bayesian learning for recovery of block-sparse signals," *IEEE Trans. Signal Process.*, vol. 63, no. 2, pp. 360–372, Jan. 2015.
- [32] S. Som and P. Schniter, "Approximate message passing for recovery of sparse signals with Markov-random-field support structure," Washington, USA, Jul. 2011.
- [33] M. Zhang, X. Kuai, F. Wang, and X. Yuan, "Variance state propagation for channel estimation in underwater acoustic massive MIMO-OFDM with clustered channel sparsity," in *Proc. IEEE/CIC Int. Conf. Commun. Workshops China (ICCC)*, Xiamen, China, Jul. 2021, pp. 233–238.
- [34] *Study on New Radio (NR) to support non-terrestrial networks*, Std. TR 38.811 V15.4.0 Release 15, 3Gpp, Spet. 2020.